Magnetic 2D Data Processing, Magnetic 3D Structure Detection Analysis, and Manual Interpretation Mapping at Netalzul Mountain, British Columbia for Jaxon Mining Inc.

May 2021

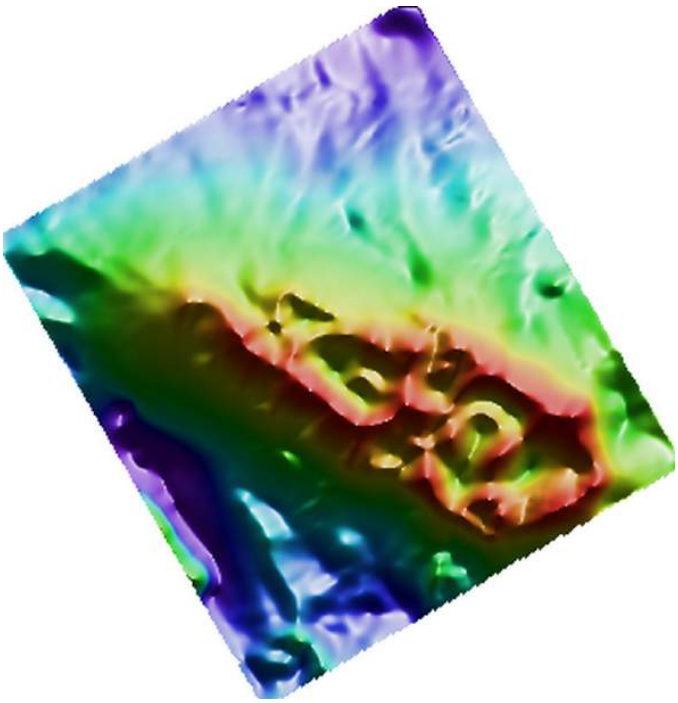

by Dan Core† and Sarah Belfield
Fathom Geophysics

†Corresponding author: dan@fathomgeophysics.com

DOCUMENT SECTION	PAGE

Introduction

This report describes processing and interpretation of magnetic data over the Netalzul Mountain area in British Columbia. The location of the project area of interest (AOI) is shown in **Figure 1**.

The goal of the work outlined in this report is to:

- carry out 2D structure detection on the gridded magnetic data over the area to highlight potential faults and contacts,
- carry out 3D structure detection on the project area's magnetic inversion model to highlight fault planes and contacts in 3D so that dips could be visualized,
- carry out a manual interpretation of the project area's magnetic structures informed by the 2D and 3D structure detection, and
- use these results with geochemical footprint modeling to highlight areas with potential to host porphyry copper mineralization.

The 2D magnetic data are from a survey flown in November 2020 by Axiom Exploration Group. The data for the surveys showed significant flight-line parallel corrugations that were removed using a frequency domain decorrugation filter. The data were provided to Fathom Geophysics with coordinates in WGS84 UTM Zone 9N. All outputs of our work use this coordinate system. Survey data have 100m line-spacing. All gridded products use a cell size of 25m.

The inversion model, which was completed by the airborne survey contractor, was supplied to Fathom Geophysics as a magnetic vector inversion. The contractor generated the inversion using Geosoft VOXI software.

The inversion has three components: the amplitude of the magnetization vector (Jaxon_mvi_amp), the component of the magnetization vector parallel to the ambient magnetic field (Jaxon_mvi_para) and the component of the magnetization vector perpendicular to the ambient magnetic field (Jaxon_mvi_perp).

All processing was completed on the amplitude voxel model. The model delivered by the airborne contractor had variable Z-spacing. Our 3D structure detection algorithm requires uniform Z-spacing, so the voxel model was resampled to a uniform Z-spacing of 18m.

Processing summary — Magnetic 2D data

Reduction to the pole (RTP)

RTP processing produces a magnetic field that is equivalent to what would be generated if the data were collected at the magnetic north pole. This takes magnetic highs in the residual magnetic intensity data (**Figure 2**) and shifts them so that they are situated directly over their sources and creates symmetric anomalies over the top of symmetric magnetic sources. The RTP filter for these data uses an inclination of 73.7° and a declination of 18.1° (**Figure 3**).

Note that in general RTP processing is not valid for remanent bodies unless the remanence is directly opposed to the present-day field. The dataset contains several remanently magnetized bodies that may not be corrected properly by the RTP filter. These areas are shown as part of the interpretation of the data in **Figure 33** of this report.

The issues with remanence led to us using the analytic signal as the input to the structure detection processing and as the basis for most of the interpretation because the analytic signal is relatively independent of remanent magnetization. The amplitude output of the MVI should also be relatively unaffected by remanent magnetization.

Magnetic standard filtering

The RTP grid was filtered with a suite of standard geophysical filters including the analytic signal and vertical derivative. These grids were imaged using our in-house software to produce shaded images with the sun coming from the north-northeast or west-northwest (NNE or WNW in the filename). Unshaded images were also produced so that the geographic location of pertinent features in the data can be readily defined (because shaded images can ‘fool the eye’ in this respect).

Figures 4 to 22 show images of most of the standard filtering results supplied. Standard filtering results have been included in this report because of their capacity to help the reader who might be new to the delivered processing results files to quickly grasp the project area’s overall magnetic susceptibility changes/contrasts.

Processing summary — Magnetic 2D data (continued)

Magnetic 2D total structure detection

Structure detection was applied to highlight edges in the analytic signal data and in the AGC-of-the-analytic-signal data. Edges in potential field data are locales that are more likely to be faults, contacts or other structures. The structure detection algorithm and processing are described in more detail in **Appendix 1**.

Representative images of the total structure detection filtering applied to the analytic signal are shown in **Figure 23A** and **Figure 23B**. Total-structure detection filtering was applied to the analytic signal grid at minimum wavelengths of 25m, 50m, 100m, 200m, 400m, and 800m. The analytic-signal-derived total structure detection results are good at depicting relatively long-wavelength features. Structure intersection images were supplied alongside structure images.

Figure 24 shows the results of applying AGC filtering to the analytic signal grid. Representative images of the total structure detection filtering applied to the AGC-of-the-analytic-signal are shown in **Figure 25A** and **Figure 25B**. Total-structure detection filtering was applied to the AGC-of-Asig grid at minimum wavelengths of 25m, 50m, 100m, 200m, 400m, and 800m. The AGC-of-analytic-signal-derived total structure detection results are good at depicting relatively detailed features as well as more subtle features in the vicinity of high amplitude anomalies. Structure intersection images were supplied alongside structure images.

Further 2D total structure detection results files were delivered in addition to those visualized within this report, and we urge the reader to explore the entire series of results files to ensure full familiarity with the results of total structure detection processing and their possible exploration ramifications.

Processing summary — Magnetic 3D structure detection

Magnetic inversion model and 3D structure detection

The details contained in the contractor-supplied magnetic inversion model for Netalzul Mountain are most meaningfully relayed via moving images rather than static pictures. **Figure 26** contains an embedded MP4 movie of the inversion model. The movie shows an inclined northeast-looking orthgonal-section view.

3D structure detection was applied to highlight edges in the inversion model. Edges in potential field data are locales that are more likely to be faults, contacts or other structures. 3D structure detection filtering was carried out at scales of 17.5m, 35m, 70m, 140m, 280m, 500m, and 1000m.

The 3D structure detection algorithms employed in the analysis at Netalzul Mountain are an extension of algorithms routinely used in Fathom Geophysics' 2D structure detection analysis of potential field survey data. The 3D structure detection filtering involves application of an edge detection filter in 32 orientations. The edge voxel models in the 32 orientations are then combined to create a total structure voxel model, a steep structure voxel model and a flat structure voxel model. Steep and flat structures are separated because they are likely to be related to different events (e.g., different timing) or are different features (e.g., relatively flat-lying contacts versus steep faults). Separating steep and flat structures also makes vectorization easier.

As with inversion modeling results, the results of 3D structure detection are also most meaningfully relayed via moving images rather than static pictures. Representative orthogonal-section view movies of the 3D structure detection filtering results are shown in **Figure 27** (for the steep 3D structures detected), **Figure 29** (for the flat 3D structures detected), and **Figure 31** (for the total 3D structure network detected).

Representative point-set view movies of the 3D structure detection filtering results are shown in **Figure 28** (for the steep 3D structures detected) and **Figure 30** (for the flat 3D structures detected). Point set results display in planar fashion the structural features detected in the inversion model. Point set results are broadly equivalent to the vector linework obtained from 2D structure detection results when analyzing a potential field survey dataset. One can regard point set results as a combined stack of vectorization results from a multitude of 2D slices.

Further scales of 3D structure detection results files were delivered in addition to the scale visualized within this report, and we urge the reader to explore the entire series of results files to ensure full familiarity with the results and their possible exploration ramifications.

Manual structural interpretation

Layers created during manual interpretation mapping

The manual interpretation consists of several layers:

- attributed interpreted structural network at Netalzul Mountain (**Table 1, Figure 32**),
- interpreted remanent areas, (green-stippled areas in **Figure 33**),
- interpreted magnetic porphyry centers (red-stippled areas in **Figure 34**),
- interpreted non-magnetic porphyry centers (blue-stippled areas in **Figure 35**), and
- interpreted location of a collapsed caldera (black-stippled areas in **Figure 36**).

The structure network consists of polylines indicating the apparent trace of faults and contacts observed in the analytic signal and the magnetic inversion. The remaining interpretation layers are polygons.

Structural stages inferred

Table 1 shows the structural stages generally inferred to have taken place in the Netalzul Mountain region. These stages have been inferred from a thorough inspection of this project's 2D and 3D structure detection results and from inspection of the scientific literature on the topic of the geotectonic settings occurring through time for British Columbia generally and for the Skeena Arch specifically.

The interpretation was completed by starting with the structures with the most recent offset and working backwards through time to the oldest structures. Some older structures most likely have offset during more recent deformation due to reactivation. For example, some east-northeast trending features appear to be relatively early strike-slip faults. However, they are parallel to more recent normal faulting and would possibly show some normal displacement.

The sense of movement was inferred by looking at how 3D structures change with depth and by looking at changes in the analytic signal across the structure. Strike-slip faults are very nearly vertical and show some apparent lateral displacement (**Figure 37**).

Normal faults show relatively little lateral offset and show changes in wavelength or signal amplitude across the faults (**Figure 38**). Thrust faults often have significant lateral and vertical displacement and often juxtapose different rock types against one another **(Figure 39**).

Manual structural interpretation

Table 1: interpreted structural stages

Stage	Structures	Comments
1	N-S–trending faults	Earliest stage. Possibly related to stress regime prevailing at the time of oceanic island arc accretion (assuming generally eastward-dipping subduction that eventually involves a significant component of northward translation of the subducting slab). At sub-surface levels that are near the present-day surface, this stage's structures seem to have only a very subtle and sparse signature now, perhaps due to their being overprinted by later structural stages. This stage's structures seem best preserved in the deepest regions of the 3D structure detection results (at a variety of scales). Sense of movement is not readily apparent.
2	NNE-trending and NE-trending shear faults	The deep-seated N-S–trending structures mentioned in the previous stage seems to smoothly rotate around and 'morph' upwards in a connected way into these NE-trending structures. It means that the structures encapsulated in this structural stage may simply be a contemporaneous, near-surface manifestation of the stress regime that created the structures seen in what we're calling Stage 1.
3	E-W–trending shear faults	The very straight, vertically-plunging structures occurring within this structural stage may represent co-occurring conjugate shear faults generated by the stress regime that produced the structures described in what we're calling Stage 2. One particular major fault falling within this structural stage stretches from east to west across the center of the project survey area, and is very deep-tapping, according to 3D structure detection results. It could have particular relevance with respect to porphyry exploration if it has acted either as a fluid pathway or as a fluid occluding/funneling surface.
4	NW-trending thrust faults	If long-lived subduction along the west coast of ancestral North America helped create these structures, then we may be seeing the results of regional-scale northeastward-directed shortening. Within Geoscience Analyst, an arbitrary-oriented section striking at N60W and dipping to the southwest at about 80 degrees coincides well with apparent decollement surfaces of these strongly-surface-expressed structures.
5	Ring faults	May have formed just before, or perhaps at the same time as, the NE-trending normal faults. It's also possible the ring faulting followed the normal faulting. The ring faults cover a very large area and appear to represent structures created during collapse of a volcanic caldera.
6	NE-trending normal faults	In places there seems to be evidence for dextral offset of NW-trending mag highs. One of these structures cuts the strongly magnetic central area in half. It could be that the now-topographically-higher SE block became uplifted while the NW block became down-dropped.

Porphyry targeting

The general tectonic setting and the larger igneous system at Netalzul appear to be favorable for porphyry-style alteration. The area is a structurally complex zone located along a large northwest-trending fault. A large intrusive complex is present and is relatively strongly magnetic with variable remanence indicating a relatively oxidized system.

The presence of ring faults in part of the area suggests that the exposed area is relatively high up in the magmatic system. This would indicate that the porphyry emplacement level has likely been preserved in the area. Normal faulting that appears to be roughly contemporaneous with the ring faults indicates that some magma may have been placed under a locally extensional tectonic setting, which is also favorable for porphyry copper formation.

The detailed geophysical signatures of porphyry copper deposits can be complex and variable depending on what part of the system is exposed, what the host rocks are, and whether the system has been tilted. We have assumed the relatively little post-emplacement tilting has taken place in this area as the normal faults that are present appear to have relatively little offset.

In lower-sulfidation porphyry systems including most alkaline and some calc-alkaline systems, the core of the system is often a magnetic high where bornite-magnetite mineralization is preserved. In higher-sulfidation systems, this zone is often overprinted with magnetite destructive phyllic alteration. The outer halo of most porphyry systems is non-magnetic due to QSP alteration. Any magnetite-bearing skarns adjacent to porphyry systems can be strongly magnetic and can be remanently magnetized.

Though the signatures can be complex, most porphyry systems are somewhat round in appearance in magnetic data. Therefore, we highlighted possible magnetic and non-magnetic porphyry centers as discrete round bodies in the analytic signal.

These centers were then evaluated based on structural setting. Finally, the targets generated using porphyry footprint modeling were examined with the interpreted porphyry centers evaluate the quality of the targets.

Target FG-NZ-Soils-1 is just south of an interpreted remanent feature that could be a small intrusive or possibly related to alteration (**Figure 40**). The target is also located in a structurally complex area with two generations of shear zones and a normal fault interpreted.

Porphyry targeting (Continued)

The target depth is not well constrained by the geochemistry largely due to gaps directly over the target and a lack of tin analyses in the data. If possible, collecting additional data in the gap prior to drilling would improve the constraints. Representative rock samples would be better than soil samples if there is sufficient outcrop.

Collection of IP data could also help constrain the targets better. A 3D pole-dipole survey with dipole spacing of at least 50m should provide enough depth penetration to see relatively deep into the system.

If this target is to be drilled prior to additional data collection, I would recommend collaring the hole over the better-constrained part of the near surface target (FG-NZ-Soils-2) and drill to the west at a 60-70° angle. This will cross target FG-NZ-Soils-1 above the ultimate target depth but should provide information to evaluate the deep target before drilling deeper holes.

Target FG-NZ-Rocks-1 coincides with an apparent demagnetized zone in the analytic signal (**Figure 41**). This looks like an interesting target and additional sampling should be completed over this area. IP surveying could be useful if infill rock samples show anything of interest.

The targets FG-NZ-Rocks-2 and FG-NZ-Rocks-3 occur in interesting structural areas at the edge of a possible magnetic porphyry center (**Figure 42**). Both targets are also at the edge of the possible caldera in the data. These are lower priority targets, but additional sampling and alteration mapping over them would help evaluate the quality of the targets.

Three additional possible porphyry centers have been interpreted east of the area covered with existing geochemistry samples. These areas should be visited to determine if any alteration is present. Geochemical samples should be taken if the rocks show evidence of porphyry style alteration.

Any additional geochemical analyses should be completed with an analytical package including tin. Rock samples should be run using a four-acid digest and ICP-MS finish. The package should include the elements As, Bi, Cu, Li, Mo, Sb, Se, Sn, Te, Tl, and W if possible. Any soil samples should use the same digestion as was used for previous analyses with an ICP-MS finish.

Any rock samples that are collected should be representative samples and not specifically focused on high-grade veins. Post mineral intrusions should be avoided if possible.

File formats and image types delivered

The 2D grids for this work have been delivered in ER Mapper ERS format. All images have been provided in GeoTIFF format with associated MapInfo TAB files and ESRI world files. Vectors have been delivered in ESRI shapefile format. The manual interpretation vector files were delivered in shapefile format with associated thematic mapping files in QGIS QML format.

2D structure detection results have been supplied as grids, images (GeoTIFF), and polylines (vectorization of the gridded results). The polylines have been attributed with the values from the structure detection grid and the orientation of the structure calculated based on the vectorized result.

All of the 2D structure images and the 3D structure movies were made using a warm color bar (yellows through to reds). The 2D structure images were created using a linear color stretch, while the 3D structure movies were created using an equal-area color distribution (i.e., histogram equalization color stretch).

Dominant orientation images use a wraparound colorbar palette that produces the same color for 0 and 180 with a rainbow distribution for colors in between. Those orientation images that have been thresholded display only significant features and are white in locales that essentially lack structure.

Magnetic susceptibility inversion results and 3D structure detection results have been supplied as voxel models in UBC mesh/model format. The 3D structure detection results have been vectorized to point sets in CSV format. Note that MP4 movies embedded in this report are supplied for qualitative report-illustration purposes. They omit features such as scalebars and latitude/longitude tickmarks to help ensure display clarity.

Several ternary images were also created for this work. These images are generated using three separate grids to represent the red-green-blue (RGB) or cyan-magenta-yellow (CMY) channels of the output image. RGB ternary images involve color addition, analogous to how different-colored light beams combine on a performance stage. When all three channels are present in full strength, pure white is the result. (Pure black indicates all three channels are absent.) CMY ternary images involve color subtraction, similar to colors resulting from the mixing of paint pigments. When all three channels are present in full strength, pure black is the result. (Pure white indicates all three channels are absent.)

Figure 17 explains in more detail how to interpret the full gamut of colors that can turn up in ternary images.

See also the list of abbreviations and acronyms supplied in this report to help decode the information contained within a given grid/image filename.

List of acronyms and abbreviations

AGC	automatic gain control (appears in delivered file names)
AGC10	AGC when standard deviation=10 (in file names)
asig	analytic signal (appears in delivered file names)
colorbar	numerical values associated with image's color range (in file names)
CMY	cyan-magenta-yellow ternary (appears in delivered file names)
Flat	flat 3D structure detection result (appears in delivered file names)
gray	image involving grayscale colorbar (appears in delivered file names)
hgm	horizontal gradient magnitude (appears in delivered file names)
HSI	hue, saturation and intensity (appears in delivered file names)
Int	structural intersections image (appears in delivered file names)
LgeRes	large-scale residual (appears in delivered file names)
lin	linear-stretch image (appears in delivered file names)
MedRes	medium-scale residual (appears in delivered file names)
NNE	shaded image involving illumination from the NNE (in file names)
NZ	Netalzul (used in target names)
OriDom	dominant orientation image (appears in delivered file names)
Pgrav	pseudogravity (appears in delivered file names)
PgravRes	residual of pseudogravity (appears in delivered file names)
PgravResHGM	HGM of residual of pseudogravity (appears in delivered file names)
pts	3D point set (appears in delivered file names)
res	residual (appears in delivered file names)
res50_200	50m-200m residual (appears in delivered file names)
RGB	red-green-blue ternary (appears in delivered file names)
RMI	residual magnetic intensity (appears in delivered file names)
RTP	reduced-to-pole (appears in delivered file names)
SmallRes	small-scale residual (appears in delivered file names)
Steep	steep 3D structure detection result (appears in delivered file names)
Struct	structure image (appears in delivered file names)
Struct100	100m minimum wavelength structure image (in file names)
tern	ternary image (appears in delivered file names)
Thresh, thr, Th	image made via thresholding (appears in delivered file names)
tilt	tilt angle (appears in delivered file names)
TMI	total magnetic intensity (appears in delivered file names)
Total	total structure result (appears in delivered file names)
uniZ	inversion involving uniform Z-axis values (in delivered file names)
vd	vertical derivative (a.k.a. 1VD) (appears in delivered file names)
vdmhgm	vertical derivative minus HGM (appears in delivered file names)
Vec	vectorized results file (appears in delivered file names)

List of acronyms and abbreviations (continued)

vias	analytic signal of vertical integral (appears in delivered file names)
vint	vertical integral (appears in delivered file names)
WNW	shaded image involving illumination from the WNW (in file names)
X	directional derivative along X axis (appears in delivered file names)
Y	directional derivative along Y axis (appears in delivered file names)
Z	directional derivative along Z axis (i.e., vertical derivative) (in file names)

Project location map

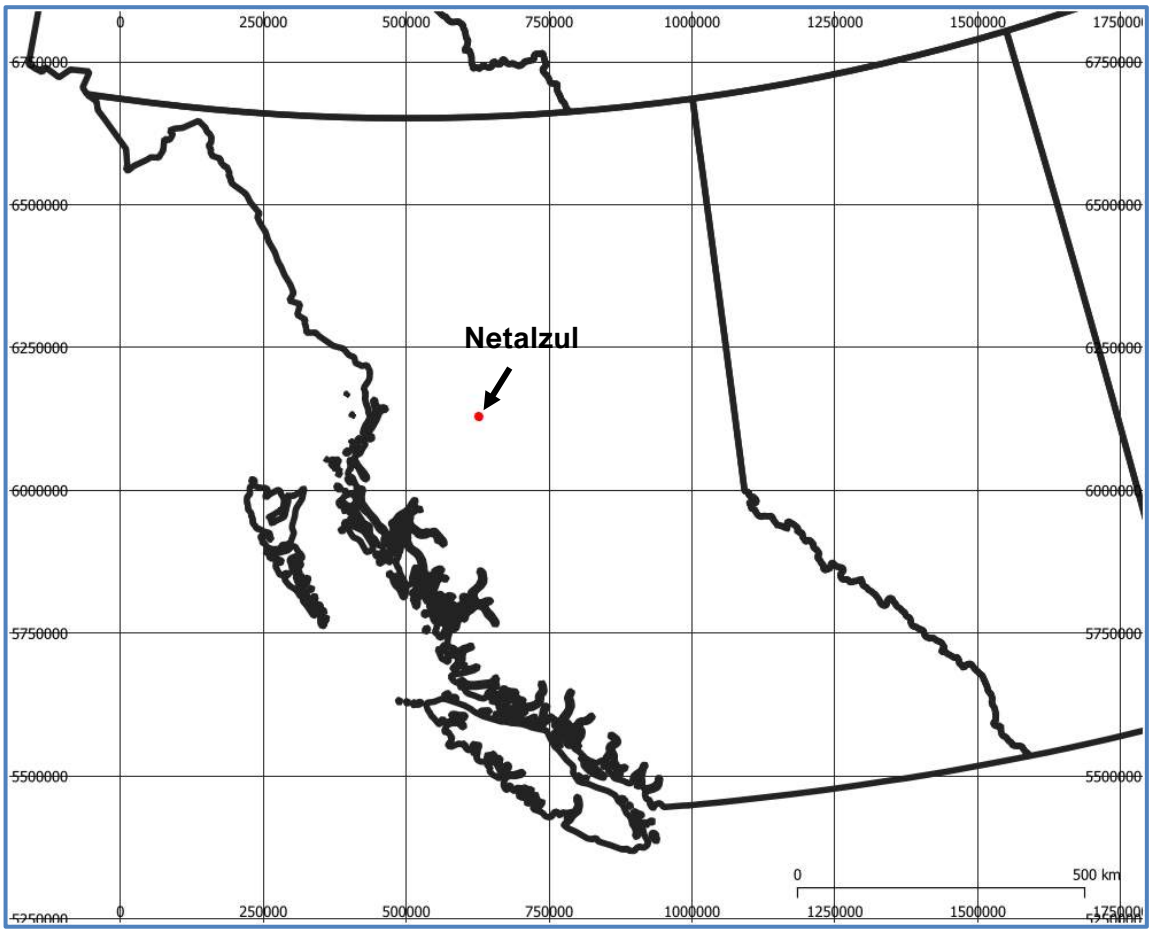

Figure 1: Map showing the location of the Netalzul Mountain project area in central BC.

Magnetic 2D data-processing results images
▶ Residual magnetic intensity (RMI)

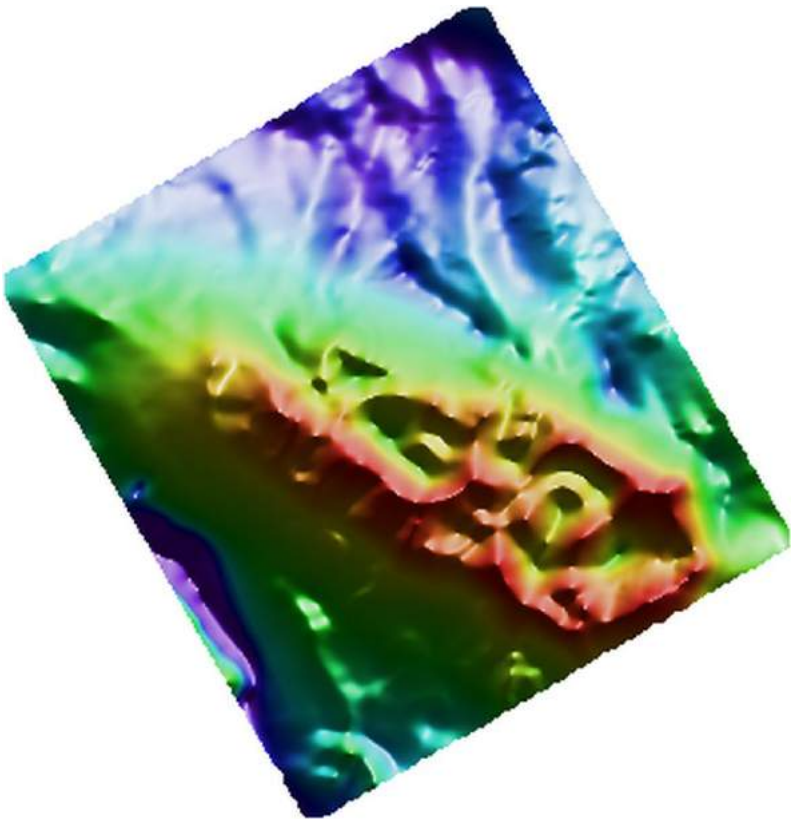

Netalzul_RMI_HSI_NNE

Low values — High values

Figure 2: Residual magnetic intensity (RMI) for the project area. The RMI is the area's total magnetic intensity (TMI) minus the international Geomagnetic Reference field (IGRF). The indicative colorbar shown applies to all magnetic data processing results images involving the HSI (hue, saturation, intensity) color display system.

Magnetic 2D data-processing results images

▶ Reduction-to-pole (RTP)

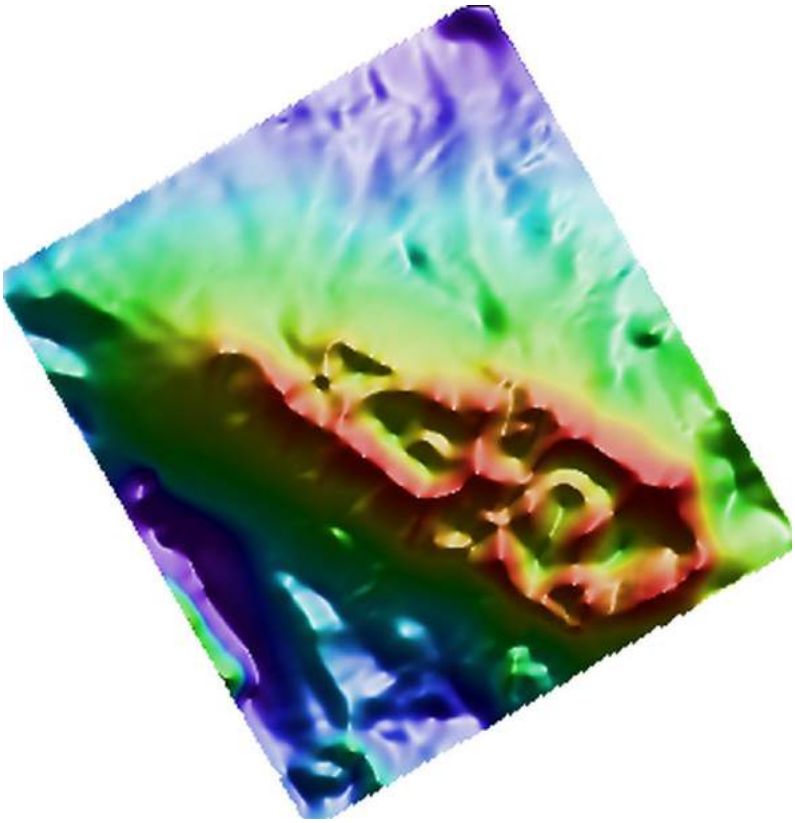

Netalzul_RMI_RTP_HSI_NNE

Figure 3: Reduced-to-the-pole magnetic data for the project area. The RTP filter attempts to produce the magnetic field that would be expected if the data were collected at the magnetic pole.

Magnetic 2D data-processing results images
▶ Standard filtering — First vertical derivative

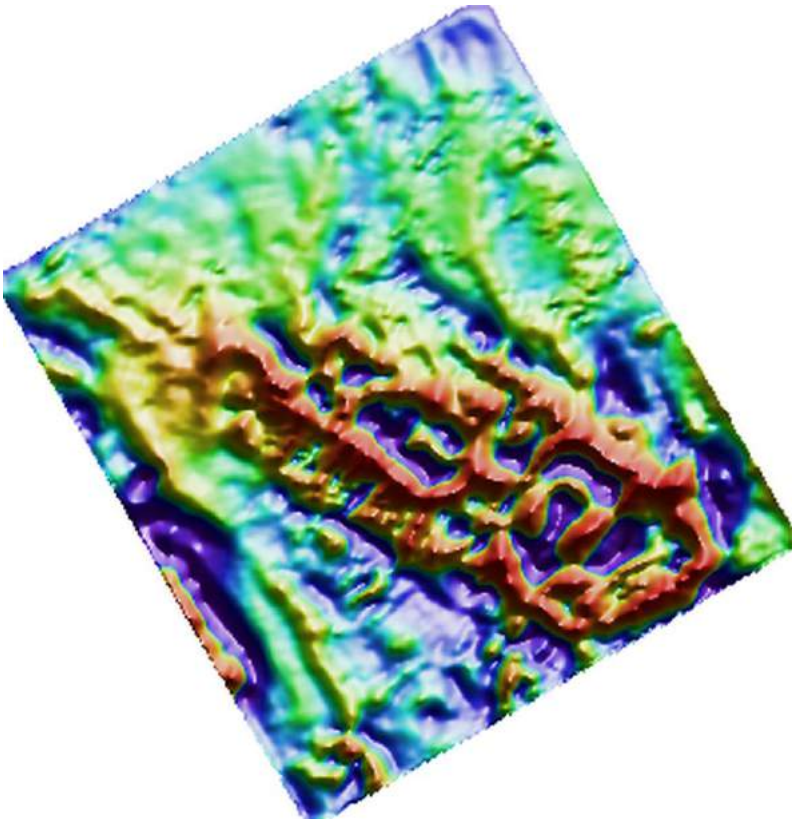

Netalzul_RMI_RTP_vd_HSI_NNE

Figure 4: The first vertical derivative (1VD) transform is the rate of change of the potential field in the vertical direction. Application of this filter has the effect of accentuating the shorter wavelength (higher frequency) components at the expense of longer wavelength (more regional) features.

Magnetic 2D data-processing results images
▶ Standard filtering — Horizontal gradient magnitude

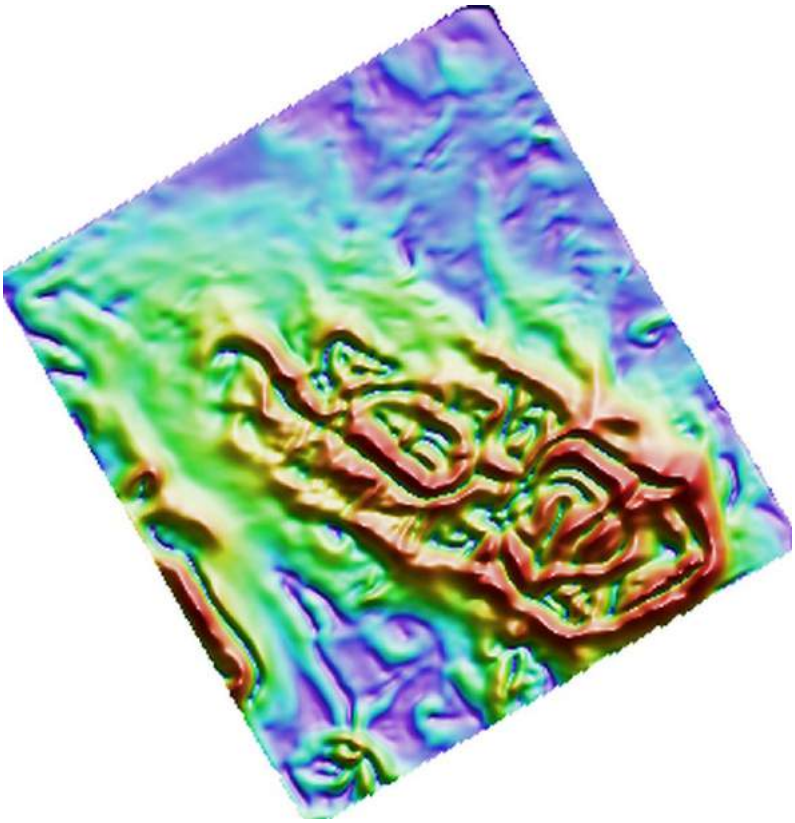

Netalzul_RMI_RTP_hgm_HSI_NNE

Figure 5: The horizontal gradient magnitude is calculated from the x- and y-derivatives of the data ($\sqrt{dx^2 + dy^2}$). This filter highlights the location of steep gradients in the data. Peaks in the HGM should occur at susceptibility contrasts in magnetic data and density contrasts in gravity data. These are likely to be locations of faults or contacts. Peaks will be offset in the down-dip direction for dipping bodies. The results are affected by remanent magnetization.

Magnetic 2D data-processing results images
▶ Standard filtering — Vertical derivative minus HGM

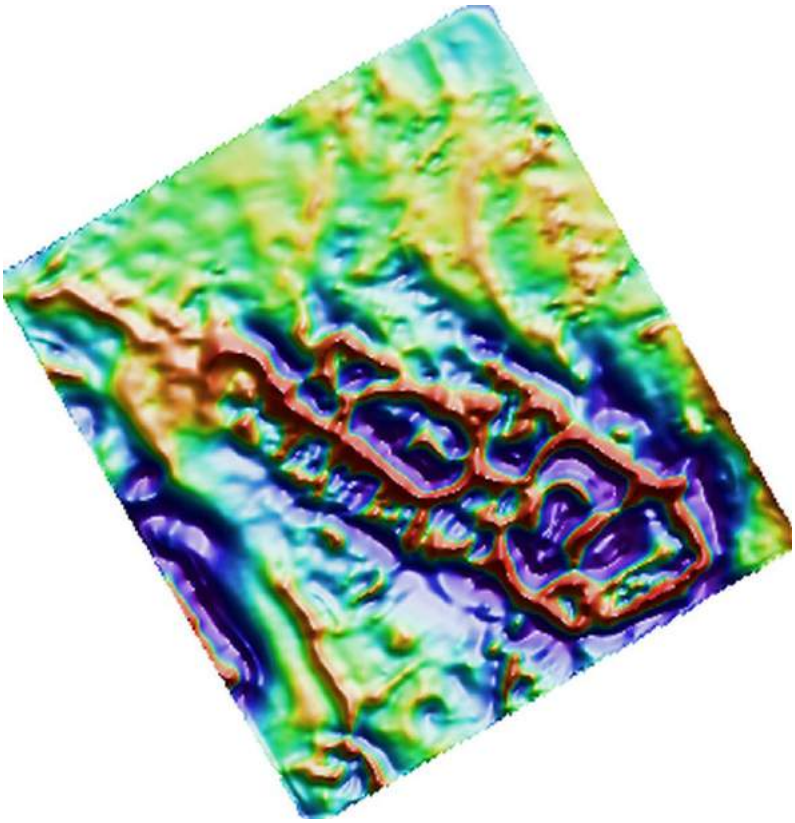

Netalzul_RMI_RTP_vdmhgm_HSI_NNE

Figure 6: The vertical derivative minus the HGM (VDMHG) is a filter that accentuates the contrast in the first vertical derivative. This is useful for highlighting shallow sources in potential field data. It can also be useful when trying to pick the exact location to place a narrow magnetic unit or a narrow dense unit.

Magnetic 2D data-processing results images
▶ Standard filtering — Tilt angle

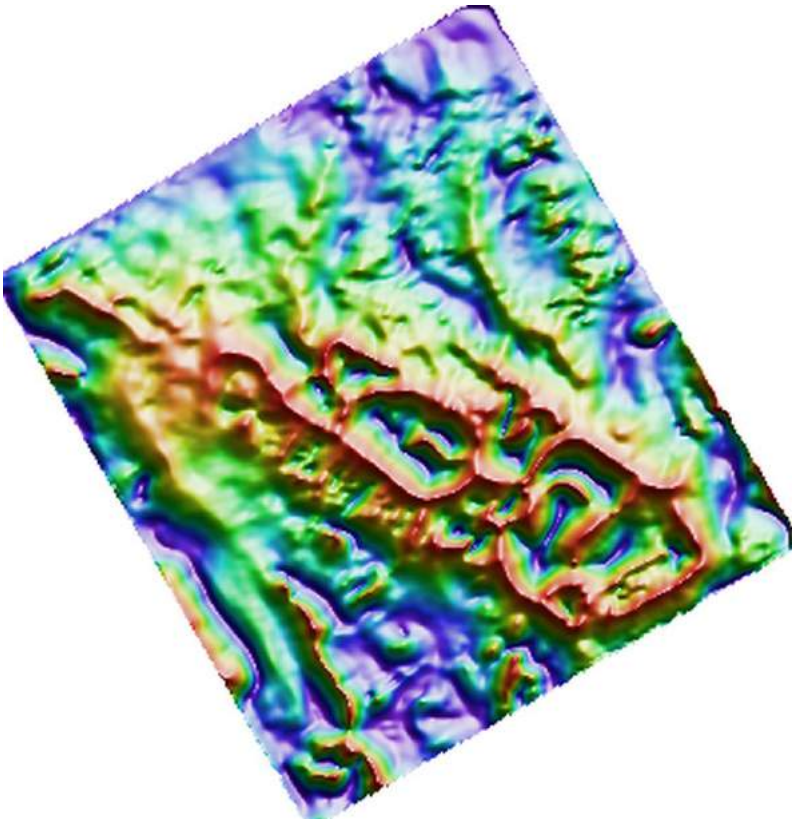

Netalzul_RMI_RTP_tilt_HSI_NNE

Figure 7: The tilt angle filter is the arctangent of the ratio of the vertical derivative to the horizontal gradient magnitude. This filter removes information about the amplitude of the signal, making the heights of peaks the same regardless of the susceptibility or density of the causative body. Structure and depth information are preserved. This makes it easier to see subtle features and some structures.

Magnetic 2D data-processing results images
▶ Standard filtering — Analytic signal

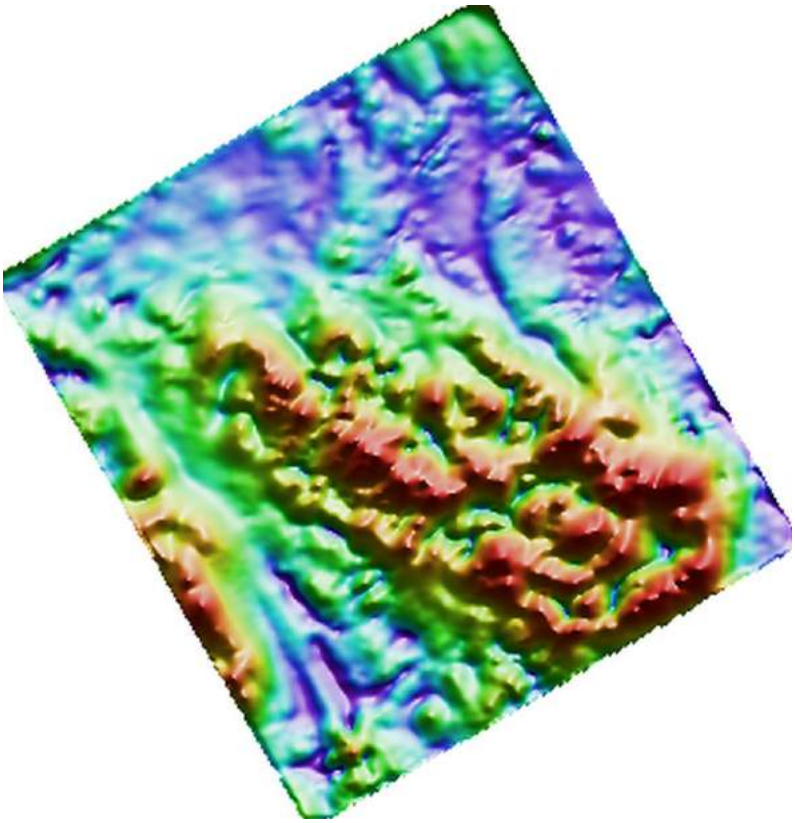

Netalzul_RMI_RTP_asig_HSI_NNE

Figure 8: Analytic signal of the RTP data. The analytic signal (also known as the total gradient magnitude) is calculated as $\sqrt{dx^2 + dy^2 + dz^2}$. This filter highlights the location of rapid changes in the data. Highs in the analytic signal correspond to high amplitudes in the vertical derivative (positive or negative) or high amplitudes in the horizontal gradient magnitude. Highs will occur over the top of small bodies with high susceptibility or high density contrast or at the edge of large-scale susceptibility or density contrast. Long-wavelength features are suppressed by this filter since it is based on derivative filters. This filter is relatively independent of magnetization direction and remanent magnetization.

Magnetic 2D data-processing results images
▶ Standard filtering — Analytic signal of vertical integral

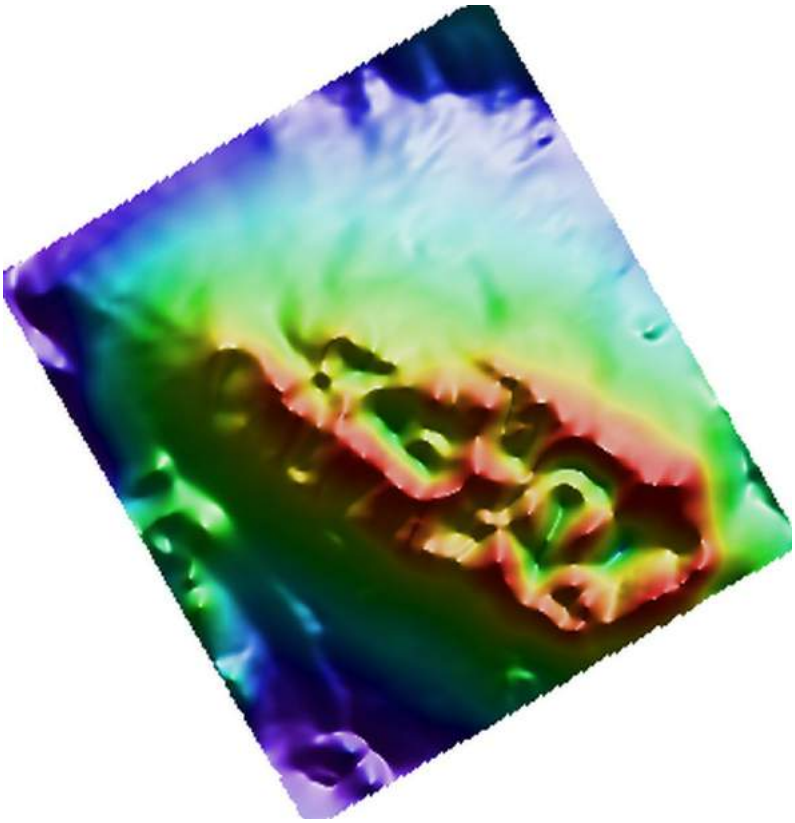

Netalzul_RMI_RTP_vias_HSI_NNE

Figure 9: The analytic signal filter was applied to the vertical integral of the magnetic data to produce this VIAS result. The analytic signal filter is described in the caption of **Figure 8**. Produces a grid with wavelength and amplitude characteristics that are similar to the RTP grid, but with reduced effects of remanent magnetization and magnetization direction.

Magnetic 2D data-processing results images
▶ Standard filtering — Automatic gain control

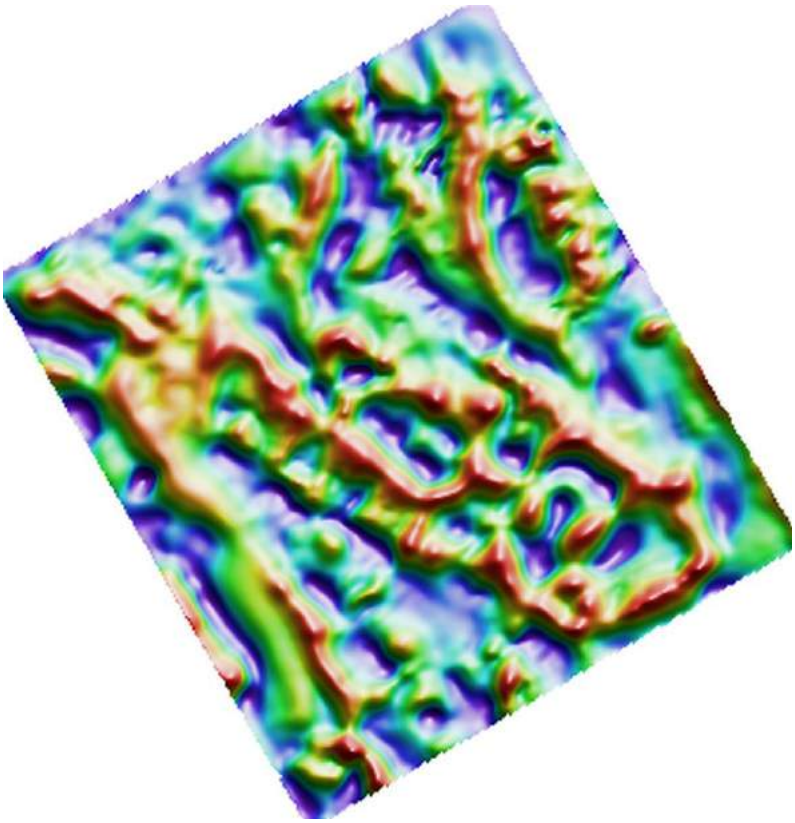

Netalzul_RMI_RTP_AGC10_HSI_NNE

Figure 10: The automatic gain control filter (AGC) is a means of evening out the amplitudes of anomalies. This makes more subtle features in the data visible. The filter also acts as a high-pass filter by suppressing the longer wavelengths.

Magnetic 2D data-processing results images
▶ Standard filtering — Small-scale residual

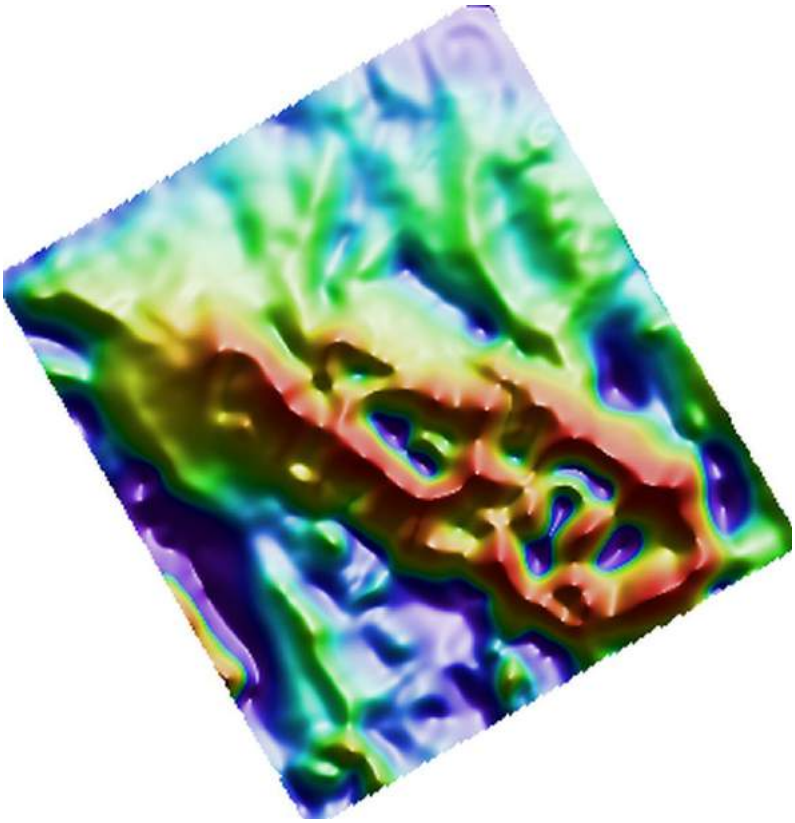

Netalzul_RMI_RTP_res50_200_HSI_NNE

Figure 11: Differential upward continuation was applied to calculate the 50m-200m residual of the RTP data in an attempt to separate sources from different depths (Jacobsen, 1987). The source depths should correspond to half of the upward continuation level. For this residual, that would be about 25m-100m depth.

Magnetic 2D data-processing results images
▶ Standard filtering — Medium-scale residual

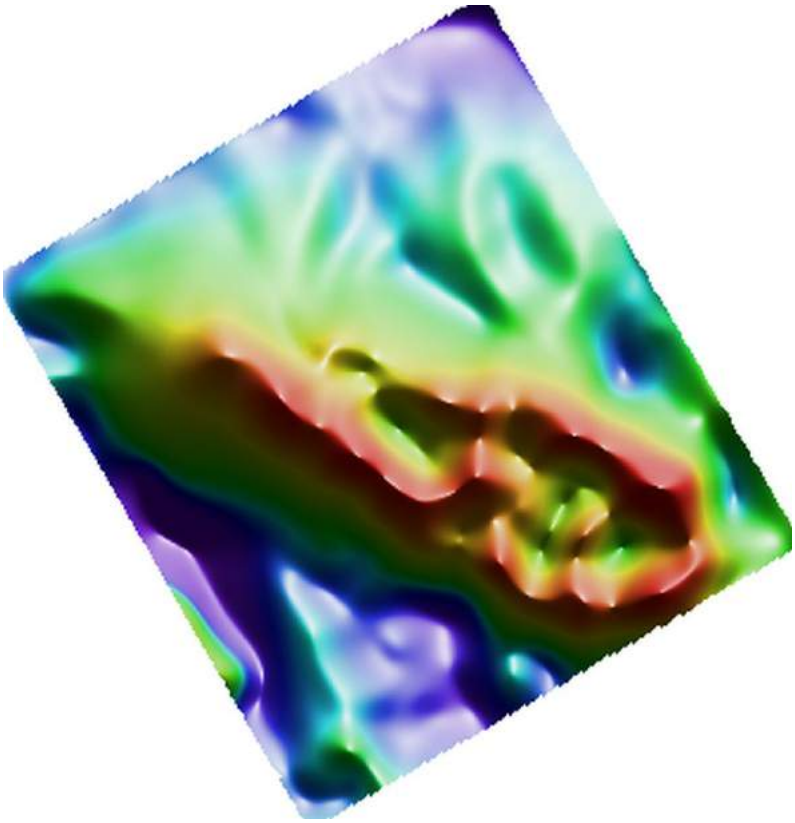

Netalzul_RMI_RTP_res200_400_HSI_NNE

Figure 12: Differential upward continuation was applied to calculate the 200m-400m residual of the RTP data in an attempt to separate sources from different depths (Jacobsen, 1987). The source depths should correspond to half of the upward continuation level. For this residual, that would be 100m-200m depth.

Magnetic 2D data-processing results images
▶ Standard filtering — Large-scale residual

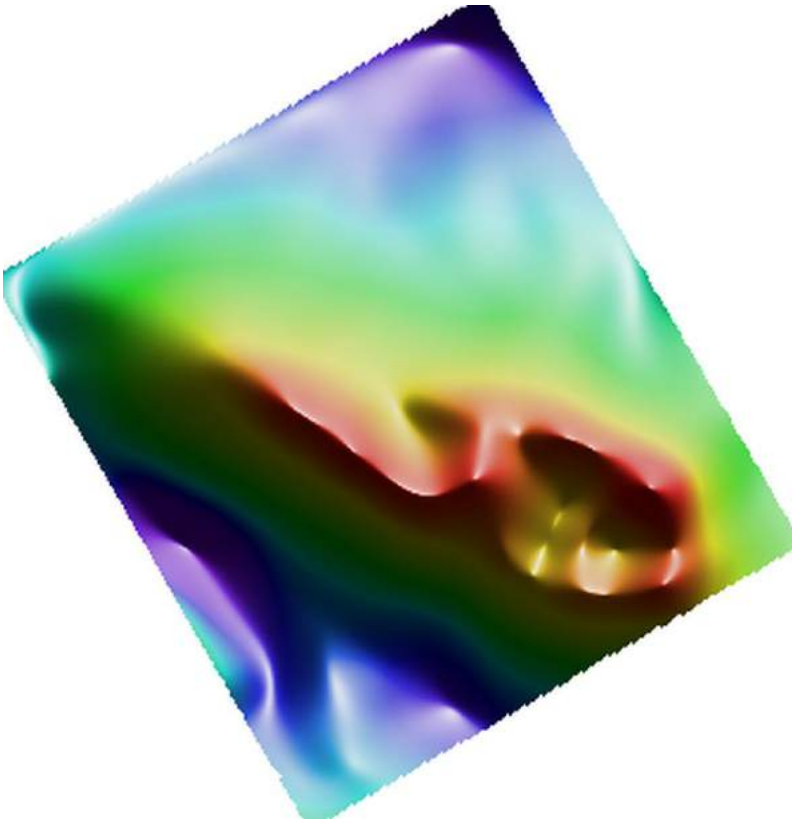

Netalzul_RMI_RTP_res400_1000_HSI_NNE

Figure 13: Differential upward continuation was applied to calculate the 400m-1000m residual of the RTP data in an attempt to separate sources from different depths (Jacobsen, 1987). The source depths should correspond to half of the upward continuation level. For this residual, that would be 200m-500m depth.

Magnetic 2D data-processing results images
▶ Standard filtering — Pseudogravity

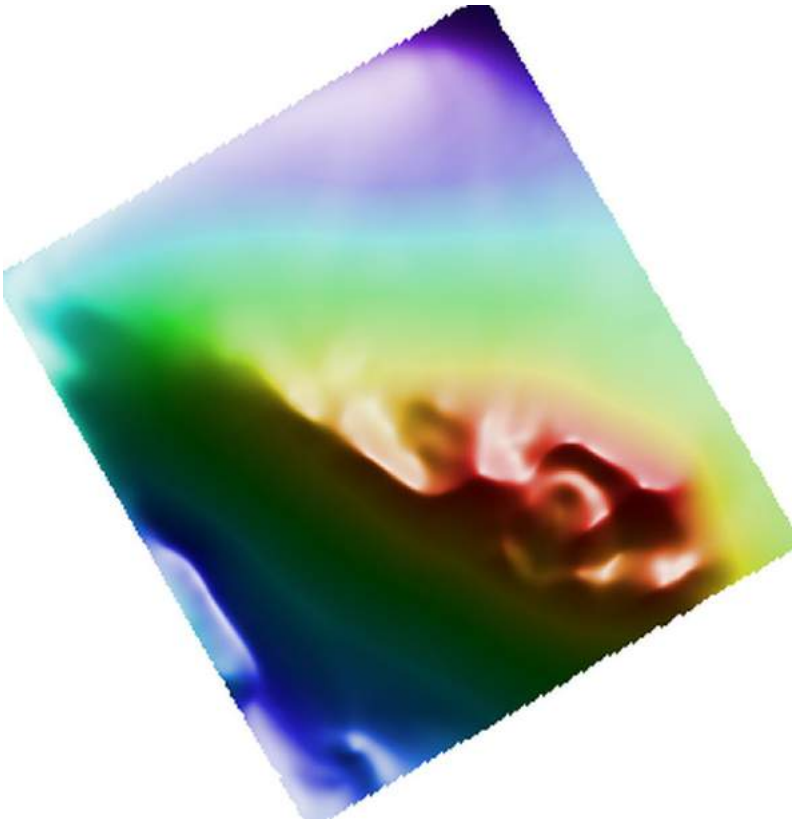

Netalzul_RMI_RTP_PGrav_HSI_NNE

Figure 14: Pseudogravity is generated by calculating the vertical integral of reduced-to-the-pole magnetic data and then using Poisson's relation (correlation between magnetic potential and gravitational potential) to scale the result. This generates a grid that is the expected gravity field if density were distributed in the same way as magnetic susceptibility in the project area. This is not a true gravity grid because it is highly unlikely that susceptibility and density are perfectly correlated. This filter enhances long-wavelength features and is good for highlighting large-scale features.

Magnetic 2D data-processing results images
▶ Standard filtering — Pseudogravity residual

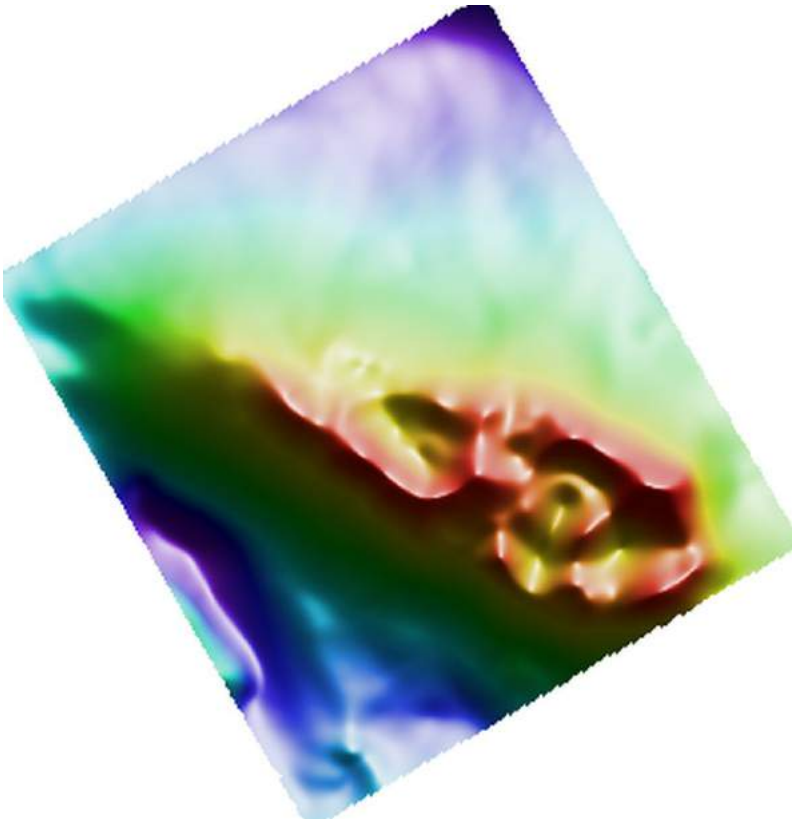

Netalzul_RMI_RTP_PGravRes_Revised_HSI_NNE

Figure 15: Differential upward continuation was applied to the pseudogravity grid to generate a 0-400m residual. This removes the longest wavelength features to allow intermediate-scale features to be seen.

Magnetic 2D data-processing results images
▶ Standard filtering — HGM of pseudogravity residual

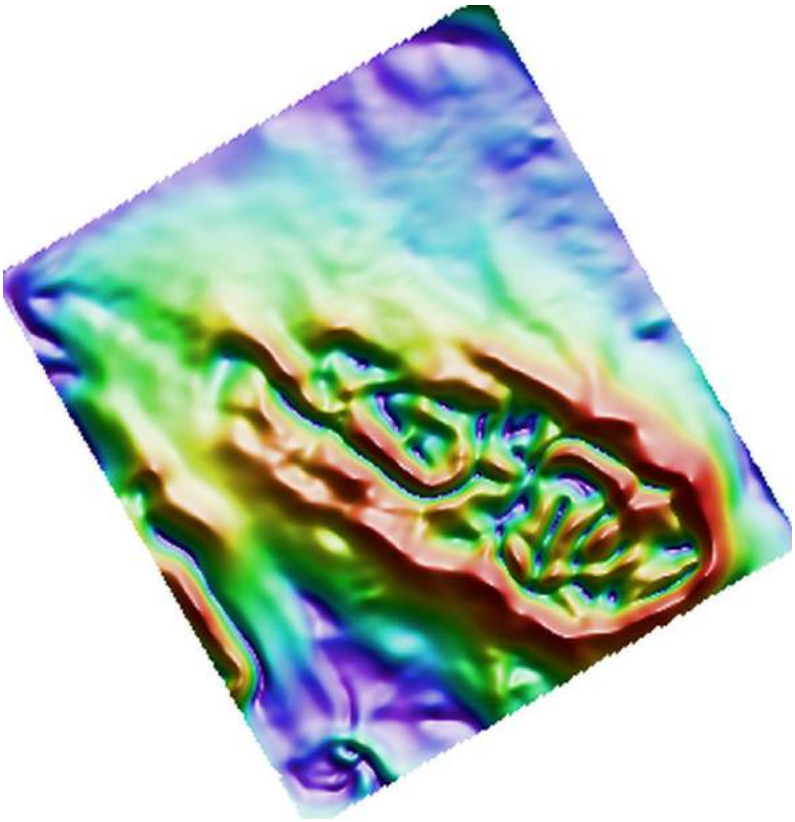

Netalzul_RMI_RTP_PGravResHGM_Revised_HSI_NNE

Figure 16: The horizontal gradient was calculated from the pseudogravity residual as described in the caption for **Figure 5**. The results highlight the edges of intermediate-scale features. However, this filter is affected by magnetization direction and remanent magnetization.

Magnetic 2D data-processing results images
▶ Standard filtering images — Using ternary images

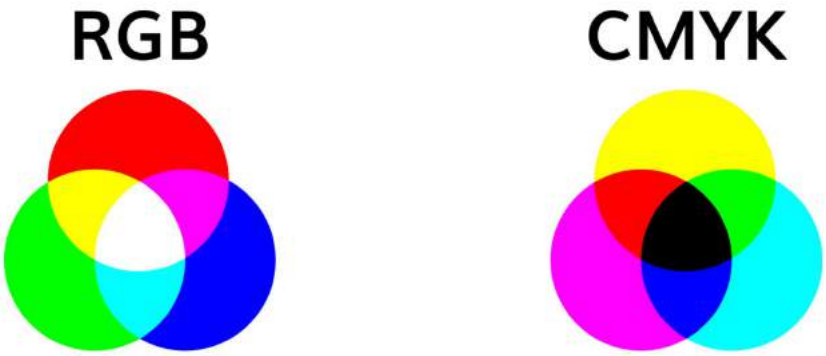

For RGB images:
Green + blue = cyan
Red + blue = magenta
Red + green = yellow
Red + green + blue = white
Low in red + green + blue = black

For CMY images:
Magenta + yellow = red
Cyan + yellow = green
Cyan + magenta = blue
Cyan + magenta + yellow = black
Low in red + green + blue = white

Figure 17: The information above shows how to interpret the colors in the RGB and CMY ternary images appearing in the next few figures, which are:

(i) Two different ternary combinations of directional derivatives — These two pairs of images encapsulate information about how steeply the gradient is changing in 3 orthogonal directions, namely the X and Y directions (within the plane of the image), and the Z direction (perpendicular to the plane of the image). All of this gradient information combines to help the observer intuitively identify the various major geological domains residing throughout the area of interest, and how these domains relate to each other.

(ii) Ternary of 1VD, tilt angle, and HGM – This image helps the observer intuitively understand where major structural features are situated, where breaks in the continuity of the magnetic 'fabric' occur, and how the textural character of the magnetic data changes from one locale to the next.

(iii) Ternary of residuals — Again, this image helps the observer intuitively understand where major structural features are situated, where breaks in the continuity of the magnetic 'fabric' occur, and how the textural character of the magnetic data changes from one locale to the next. However, features seen are generally coarser than those appearing in the ternary combining 1VD, tilt and HGM.

(iv) Ternary of RTP, analytic signal, and VIAS – This image helps the observer intuitively understand which subareas may be most affected by remanence (red locales in the CMY image).

Magnetic 2D data-processing results images

▶ Standard filtering — Ternary of directional derivatives #1

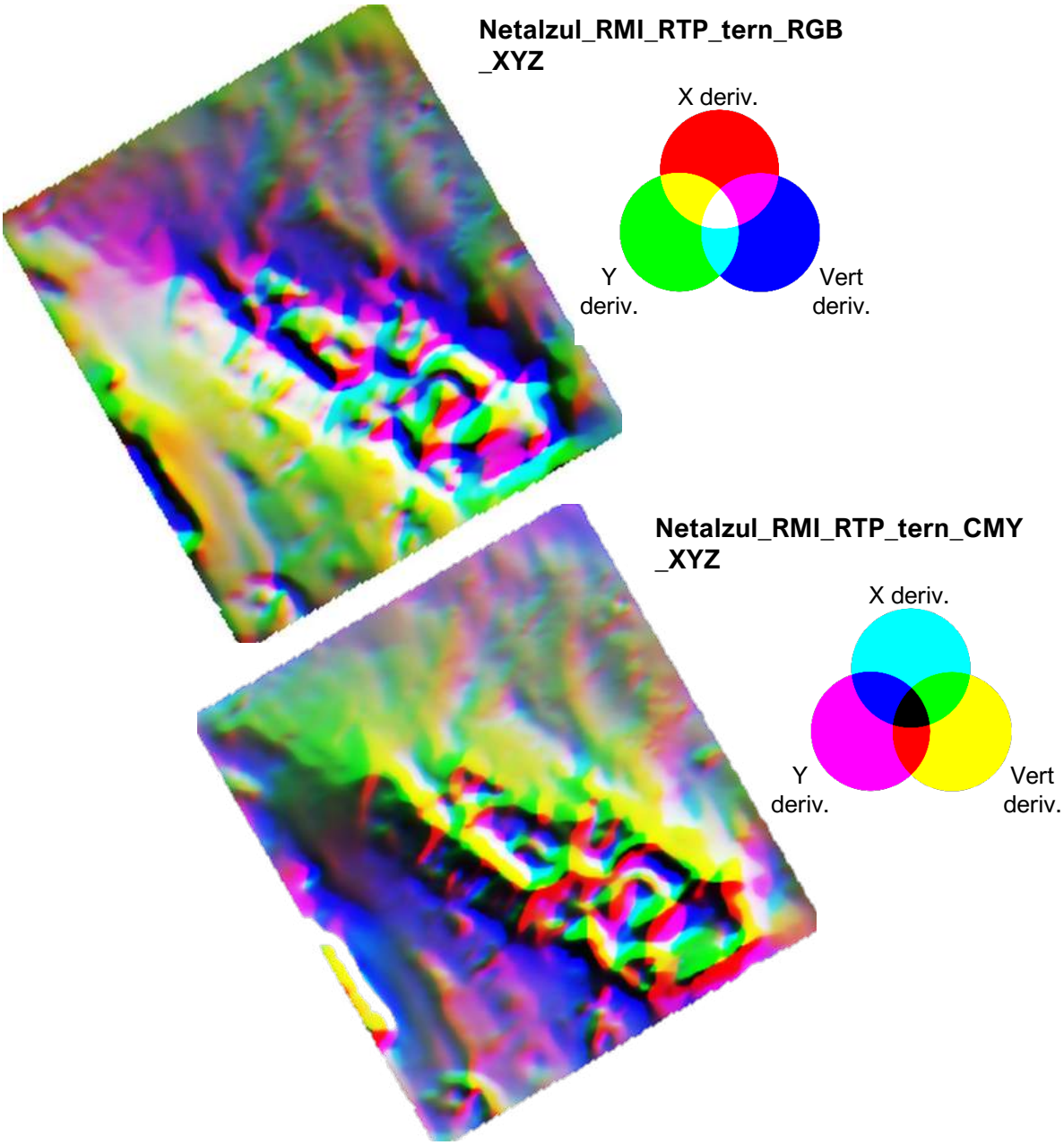

Figure 18: RGB and CMY ternary images co-displaying the X-gradient (R/C channels), Y-gradient (G/M channels), and Z-gradient (i.e., vertical derivative) (B/Y channels).

Magnetic 2D data-processing results images
▶ Standard filtering — Ternary of directional derivatives #2

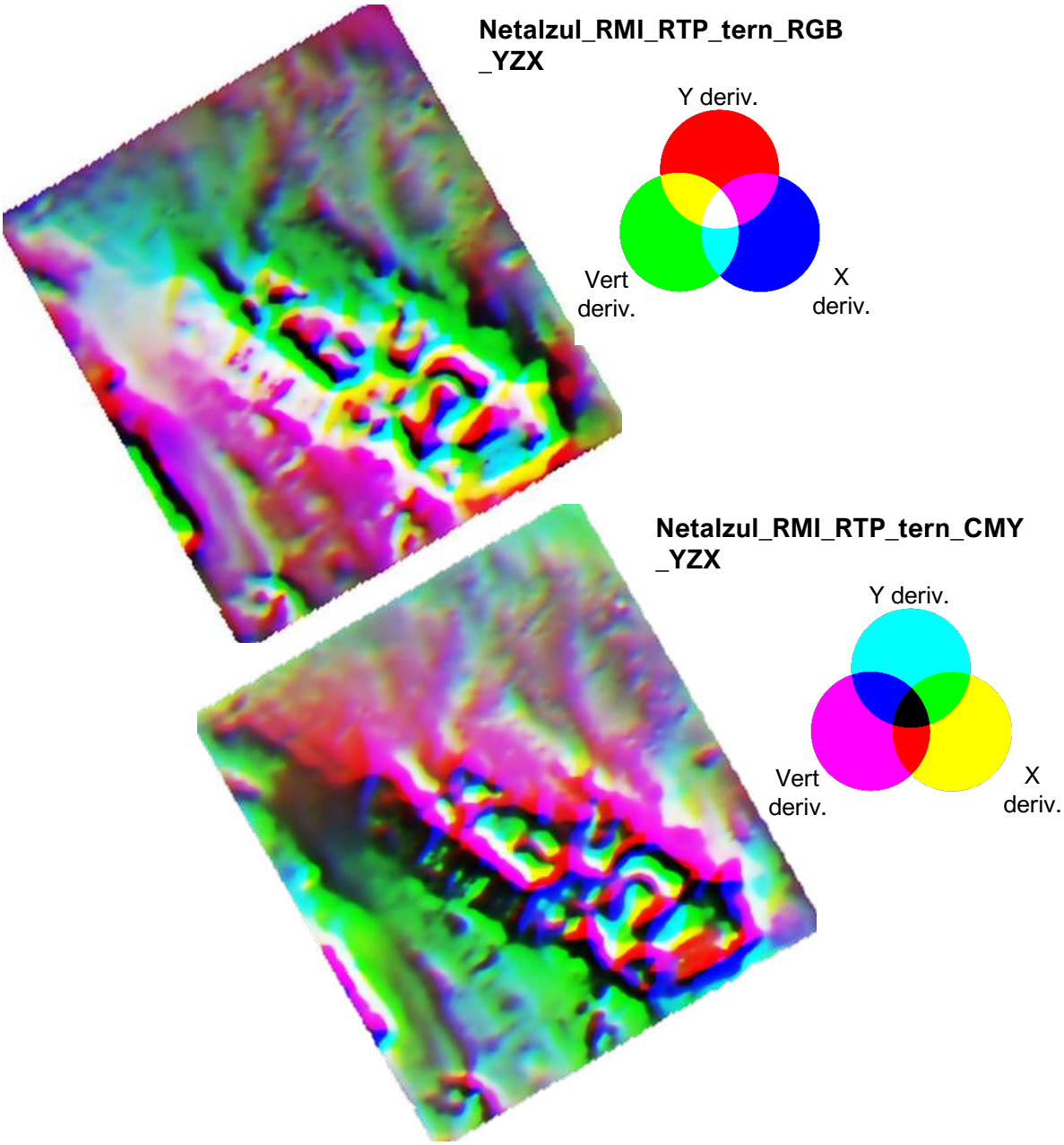

Figure 19: RGB and CMY ternary images co-displaying the Y-gradient (R/C channels), Z-gradient (i.e., vertical derivative) (G/M channels), and X-gradient (B/Y channels).

Magnetic 2D data-processing results images

▶ Standard filtering — Ternary of 1VD, tilt, HGM

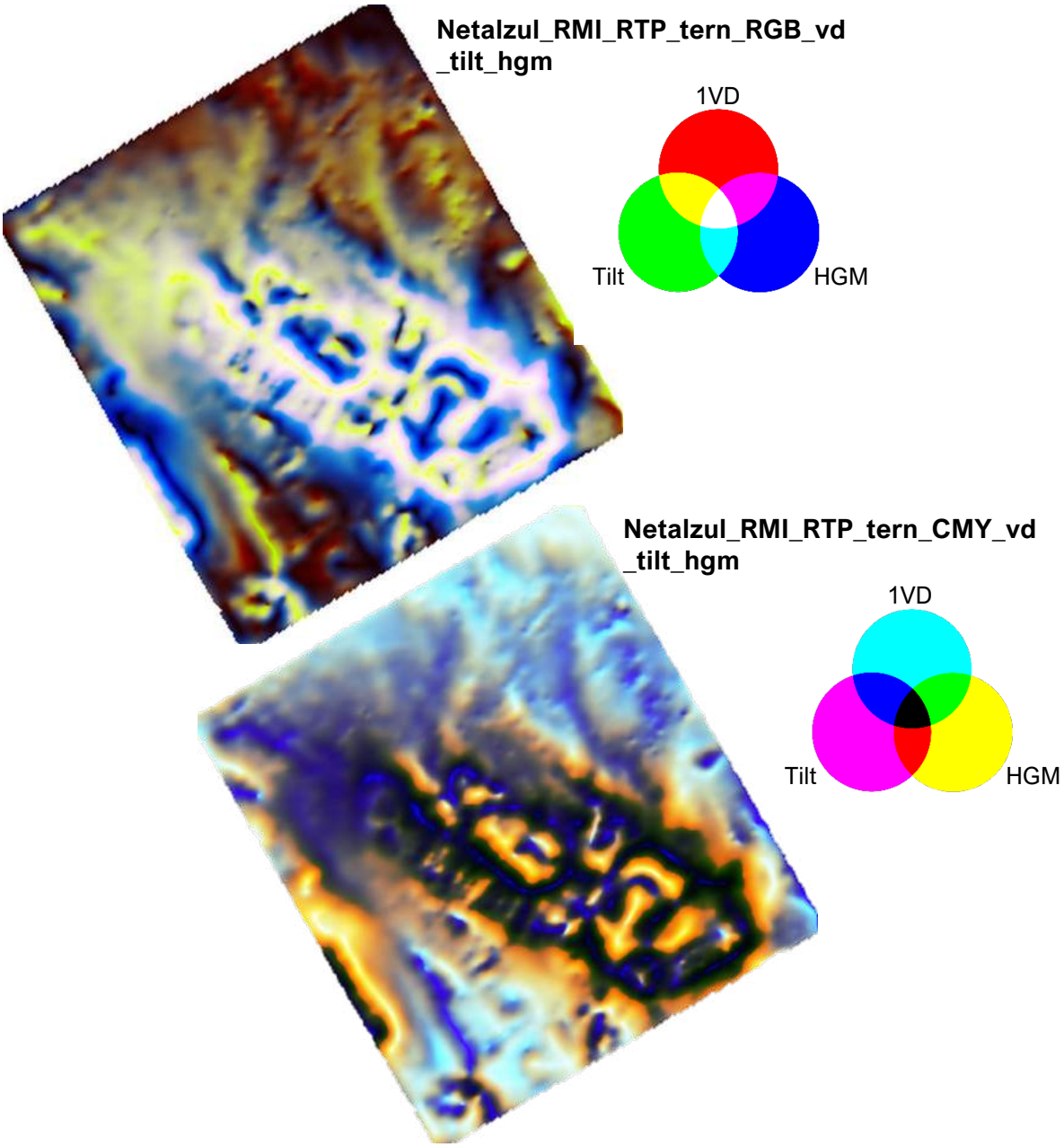

Figure 20: RGB and CMY ternary images co-displaying the vertical derivative (R/C channels), tilt angle (G/M channels), and HGM (B/Y channels).

Magnetic 2D data-processing results images
▶ Standard filtering — Ternary of residuals

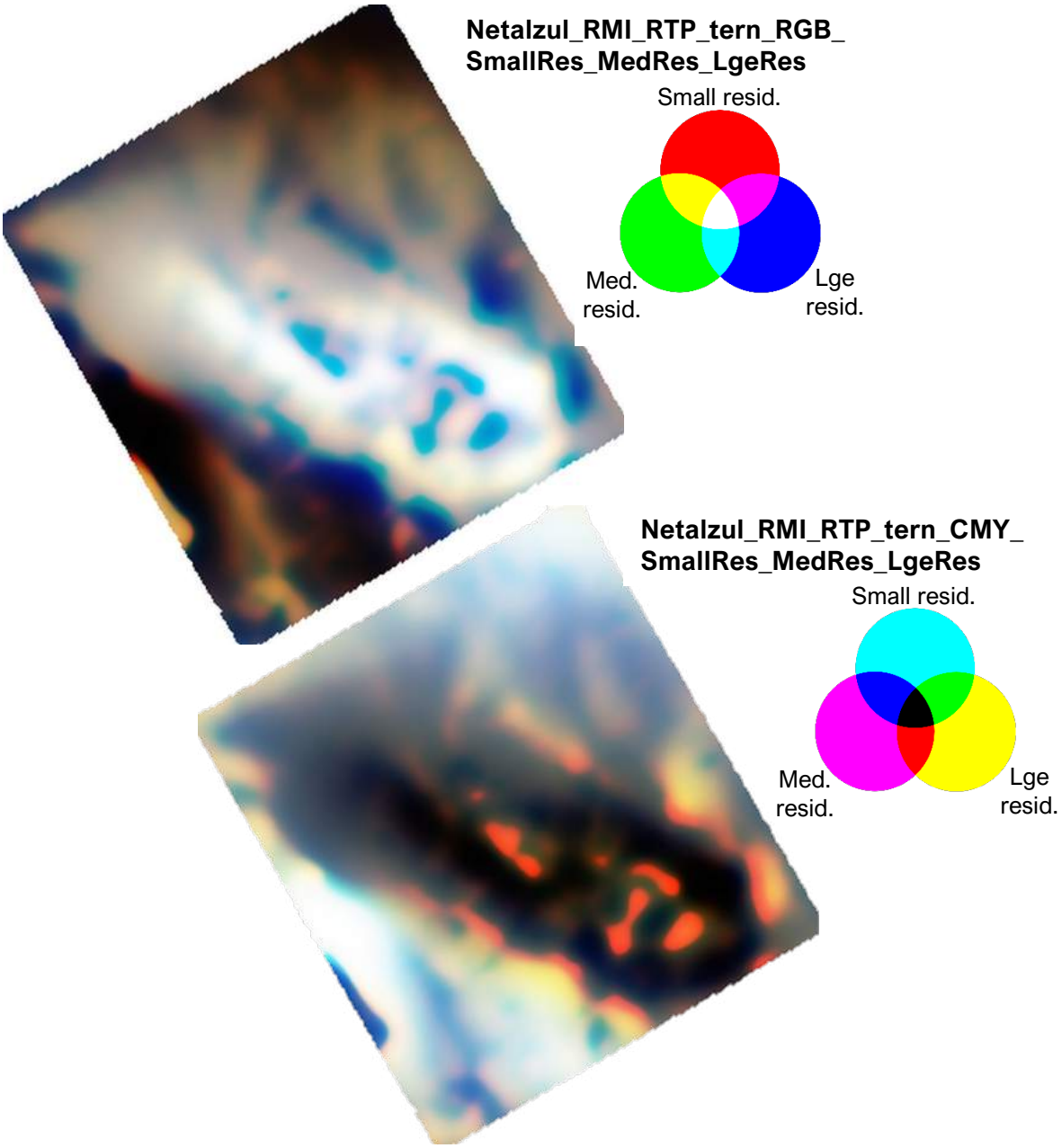

Figure 21: RGB and CMY ternary images co-displaying the small-scale (R/C channels), medium-scale (G/M channels), and large-scale residuals (B/Y channels).

Magnetic 2D data-processing results images

▶ Standard filtering — Ternary of RTP, Asig, VIAS

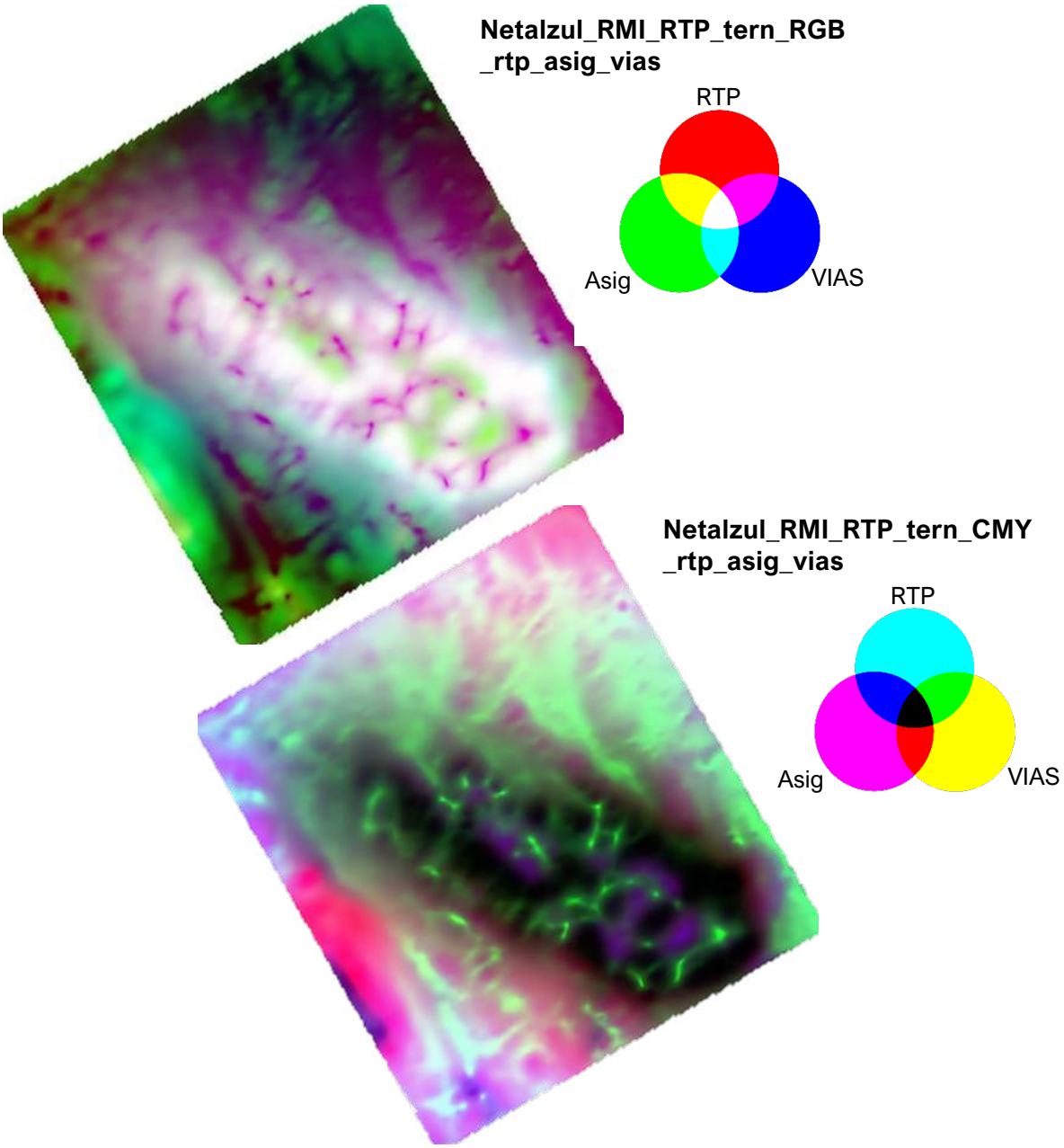

Figure 22: RGB and CMY ternary images co-displaying the RTP (R/C channels), analytic signal (G/M channels), and VIAS (B/Y channels).

Magnetic 2D data-processing results images

▶ Total structure detection — Analysis of analytic signal

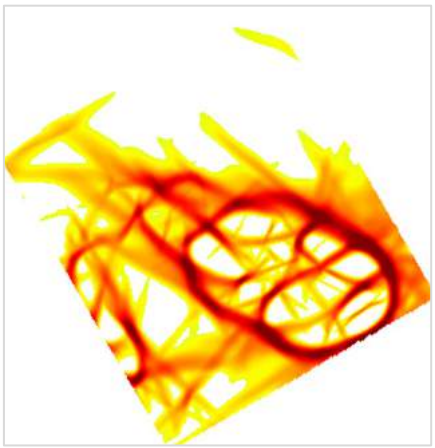

Figure 23A: Representative image** showing 200m structure detection results for the analytic signal data. TOP: Total structure detected. MIDDLE: Map of thresholded structural orientations. BOTTOM: Total structure in vectorized form (black lines with displayed thickness varying according to median value) over the project area's analytic signal image.

Netalzul_RMI_RTP_asig_Struct200_Total

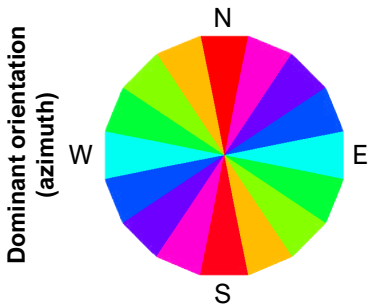

Netalzul_RMI_RTP_asig_Struct200_OriDom_Thresh

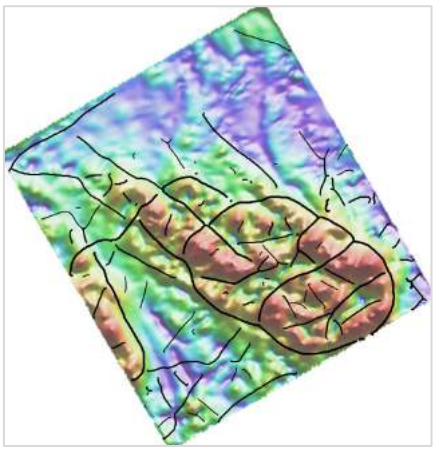

Netalzul_RMI_RTP_asig_Struct200_Total_Vec

** *Further scales of results also delivered.*

Magnetic 2D data-processing results images
▶ Total structure detection — Analysis of analytic signal

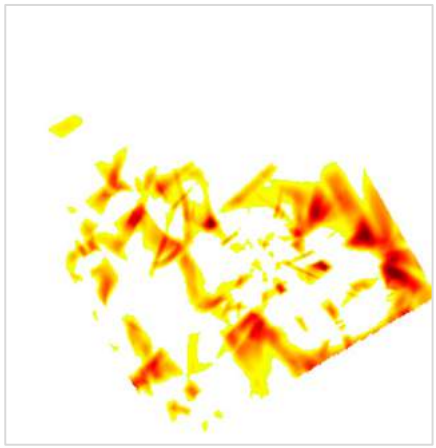

Figure 23B: Representative image** showing 200m structure detection results for the analytic signal data. TOP: Total structure intersections detected. MIDDLE: Intersections co-displayed with same-scale structures (displayed line color and thickness varies according to structure's median value). BOTTOM: Intersections co-displayed with grayscale analytic signal.

Netalzul_RMI_RTP_asig_Struct200_Int

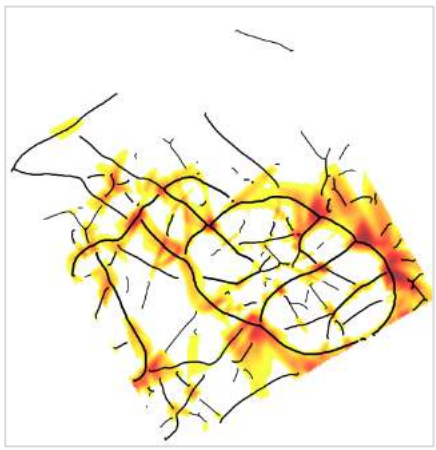

Netalzul_RMI_RTP_asig_Struct200_Int

Netalzul_RMI_RTP_asig_Struct200_Total_Vec

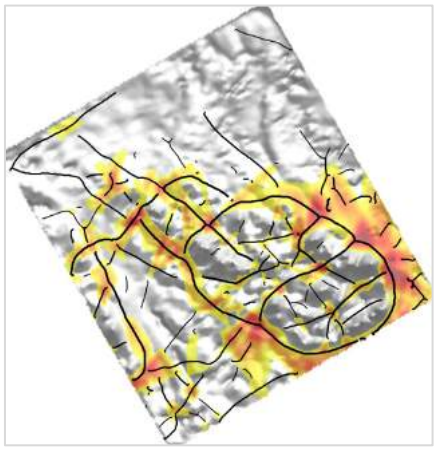

Netalzul_RMI_RTP_asig_Struct200_Int

Netalzul_RMI_RTP_asig_Struct200_Total_Vec

*** Further scales of results also delivered.*

Magnetic 2D data-processing results images
▶ Total structure detection — AGC of analytic signal

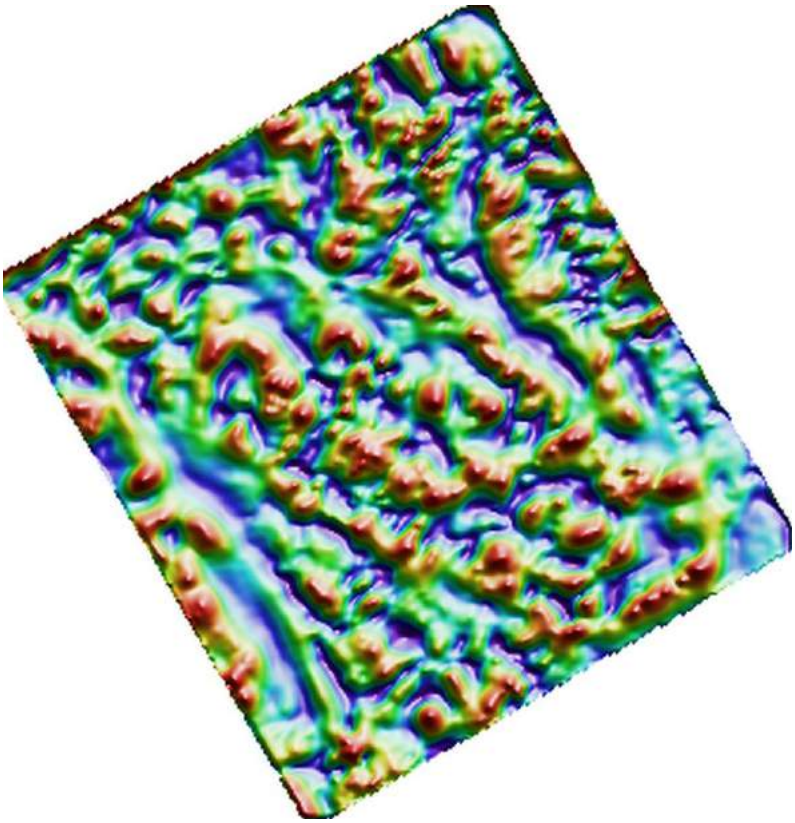

Netalzul_RMI_RTP_asig_AGC10_HSI_NNE

Figure 24: The automatic gain control filter (AGC) was applied to the analytic signal grid for the purposes of producing a second batch of structure detection analysis results. Recall that the AGC is a means of evening out the amplitudes of anomalies, making more subtle features in the data visible. The filter also acts as a high-pass filter by suppressing the longer wavelengths.

Magnetic 2D data-processing results images

▶ Total structure detection — Analysis of AGC of analytic signal

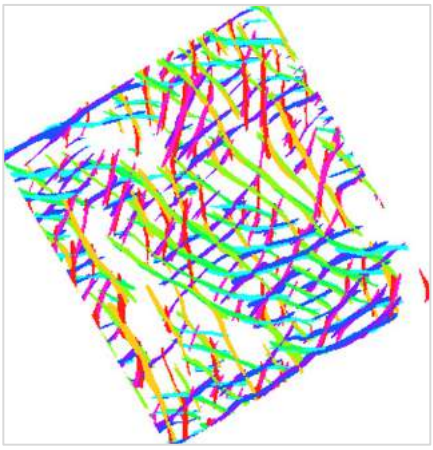

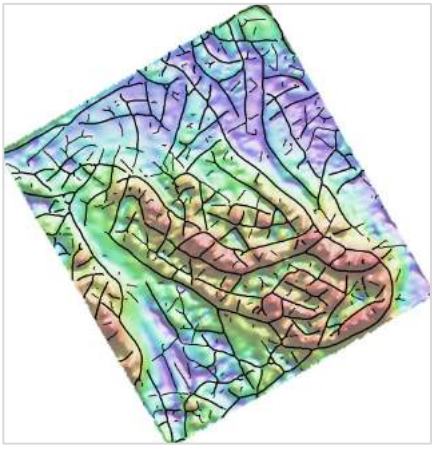

Figure 25A: Representative image** showing 100m structure detection results for the analytic signal's AGC. TOP: Total structure detected. MIDDLE: Map of thresholded structural orientations. BOTTOM: Total structure in vectorized form (black lines with displayed thickness varying according to median value) over the project area's analytic signal image.

Netalzul_RMI_RTP_asig_AGC10_Struct100_Total

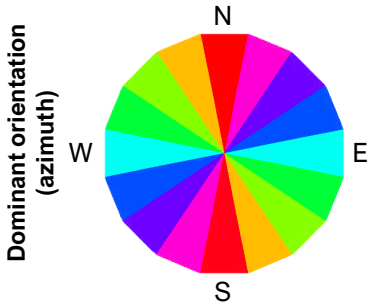

Netalzul_RMI_RTP_asig_AGC10_Struct100_OriDom_Thresh

Netalzul_RMI_RTP_asig_AGC10_Struct100_Total_Vec

*** Further scales of results also delivered.*

Magnetic 2D data-processing results images
▶ Total structure detection — Analysis of AGC of analytic signal

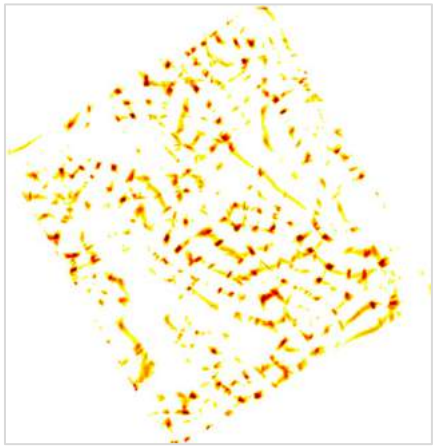

Figure 25B: Representative image** showing 100m structure detection results for the analytic signal's AGC. TOP: Total structure intersections detected. MIDDLE: Intersections co-displayed with same-scale structures (displayed line color and thickness varies according to structure's median value). BOTTOM: Intersections co-displayed with grayscale analytic signal.

Netalzul_RMI_RTP_asig_AGC10_Struct100_Int

Netalzul_RMI_RTP_asig_AGC10_Struct100_Int

Netalzul_RMI_RTP_asig_AGC10_Struct100_Total_Vec

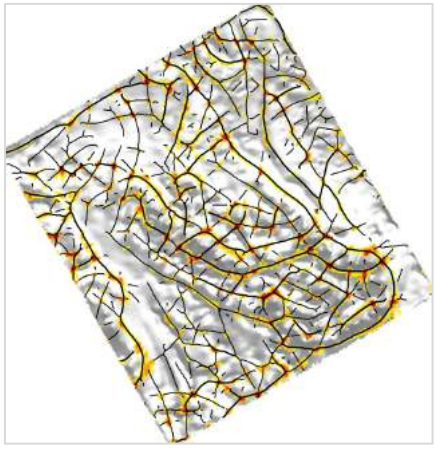

Netalzul_RMI_RTP_asig_AGC10_Struct100_Int

Netalzul_RMI_RTP_asig_AGC10_Struct100_Total_Vec

*** Further scales of results also delivered.*

Magnetic 3D structure detection results images

▶ Inversion model in section view

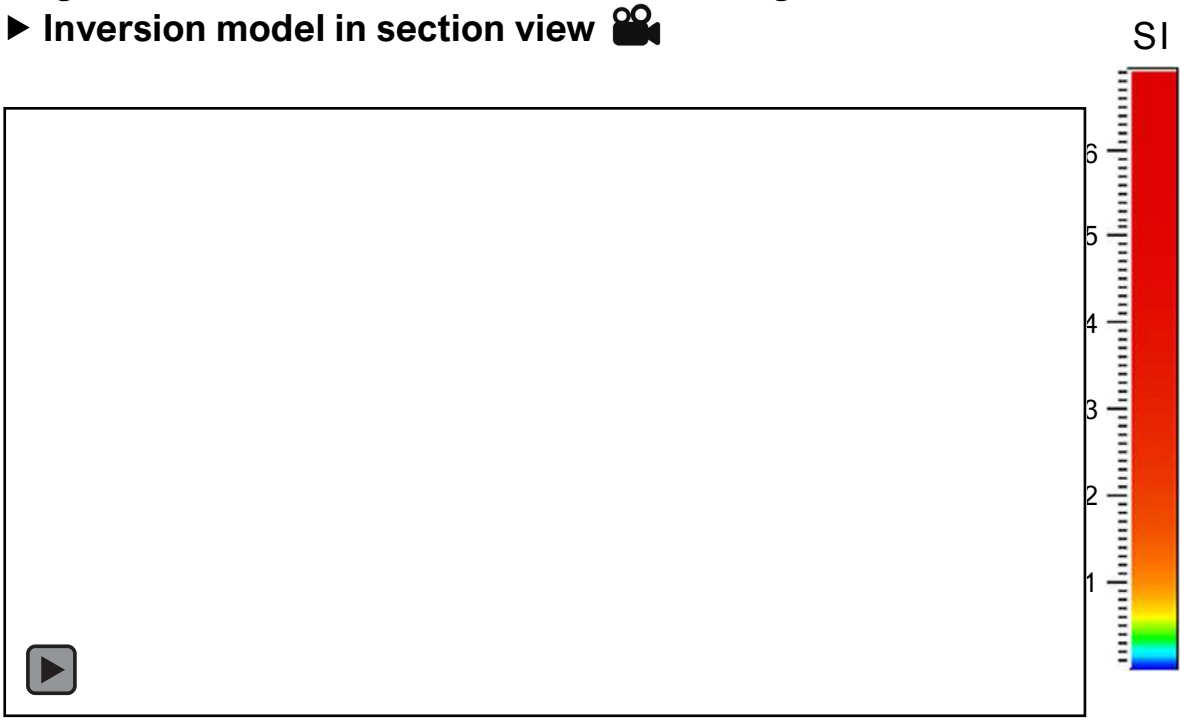

Jaxon_mvi_amp_uniZ

Figure 26: Movie (MP4, 2.1MB, 33 sec) of the Netalzul Mountain magnetic inversion model. This voxel grid result is shown looking toward the northeast, with a viewing inclination of 45°. This a movie of the Geoscience Analyst graphic user interface. First, the north-south–trending section is shifted back and forth across the cube. Then the east-west–trending section is shifted. Last of all the horizontal section is raised and lowered through the display cube's extent.

Magnetic 3D structure detection results images
▶ Steep 3D structures — Voxel grid in section view

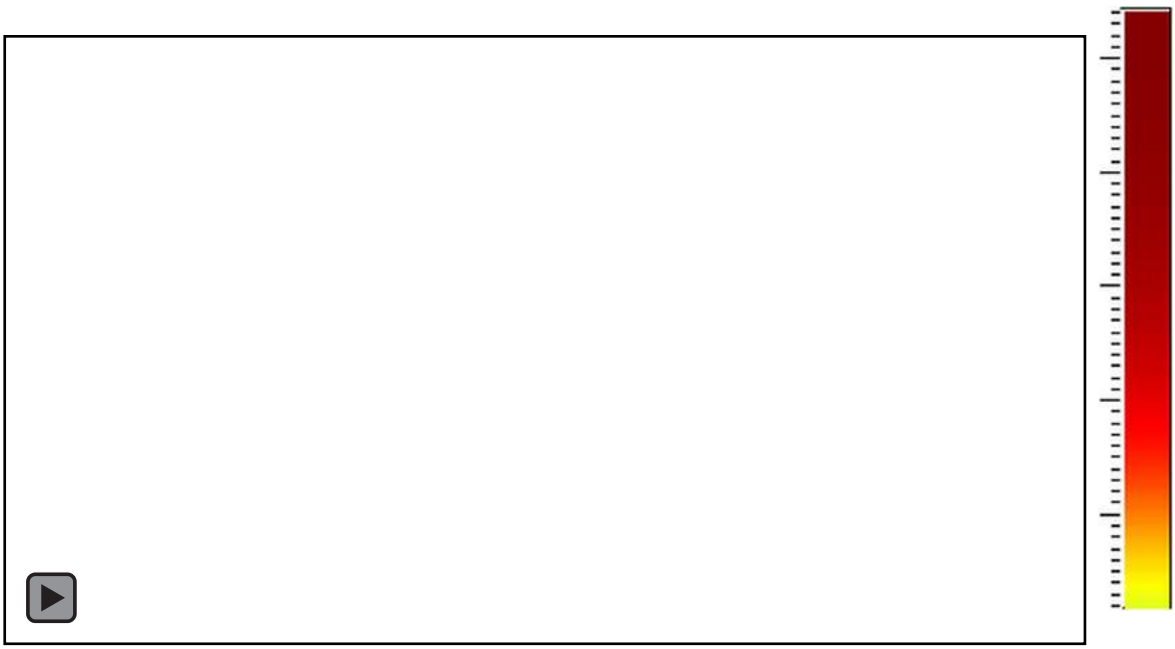

Jaxon_mvi_amp_uniZ_Struct140_Steep

Figure 27: Movie (MP4, 2.4MB, 30 sec) of a representative image** showing the 140m-scale steep 3D structures detected in the Netalzul Mountain magnetic inversion model. This voxel grid result is shown looking toward the northeast, with a viewing inclination of 45°. This a movie of the Geoscience Analyst graphic user interface. First, the north-south–trending section is shifted back and forth across the cube. Then the east-west–trending section is shifted. Last of all the horizontal section is raised and lowered through the display cube's extent.

** *Further scales of results also delivered.*

Magnetic 3D structure detection results images

▶ Steep 3D structures — Point set results view

Jaxon_mvi_amp_uniZ_Struct140_Steep_pts

Figure 28: Movie (MP4, 220KB, 10 sec) of a representative image** showing the 140m-scale steep 3D structures detected in the Netalzul Mountain magnetic inversion model. These point set results are shown looking toward the northeast, with a viewing inclination of 79°. This movie's Geoscience Analyst stills are:

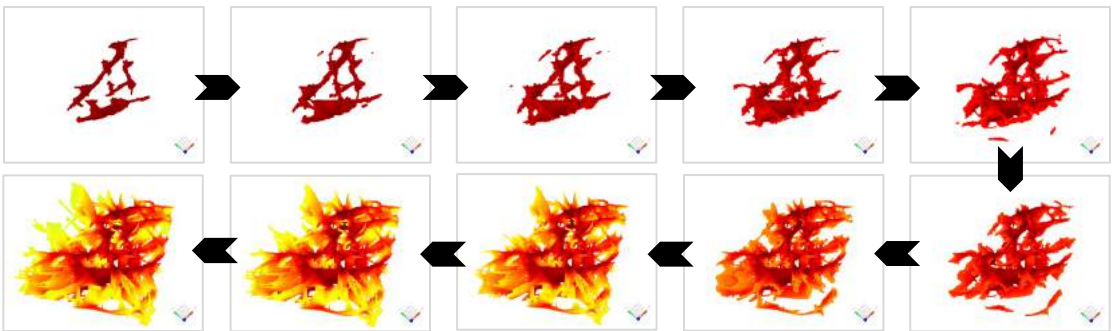

** *Further scales of results also delivered.*

Magnetic 3D structure detection results images

▶ Flat 3D structures — Voxel grid in section view

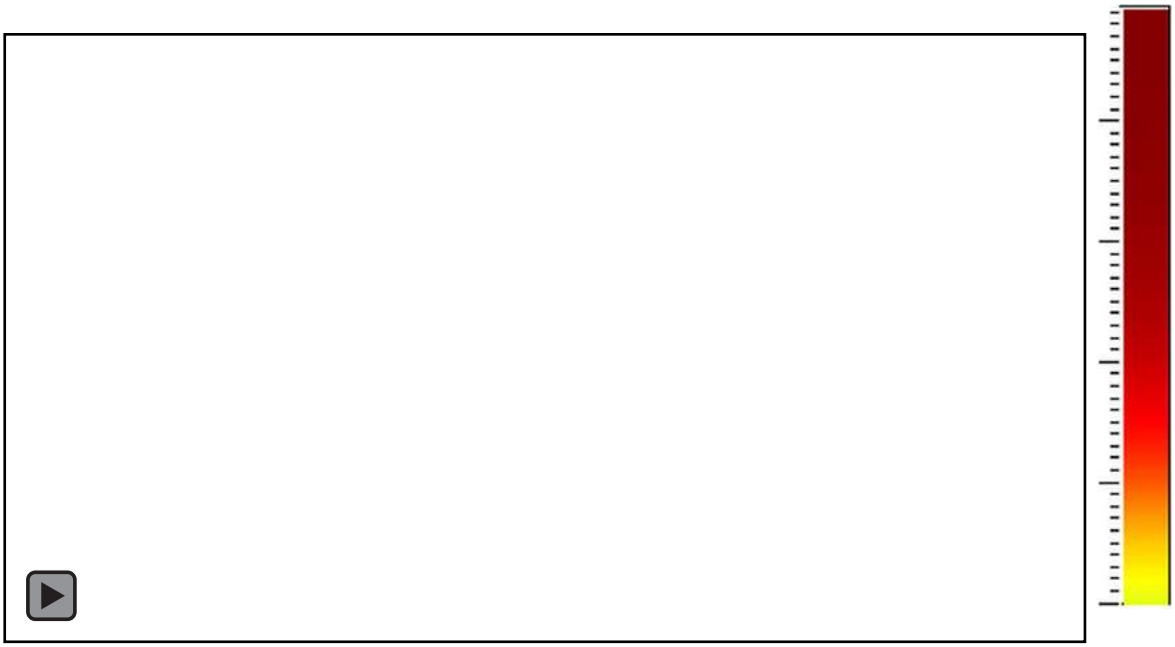

Jaxon_mvi_amp_uniZ_Struct140_Flat

Figure 29: Movie (MP4, 2.4MB, 31 sec) of a representative image** showing the 140m-scale flat 3D structures detected in the Netalzul Mountain magnetic inversion model. This voxel grid result is shown looking toward the northeast, with a viewing inclination of 45°. This a movie of the Geoscience Analyst graphic user interface. First, the north-south–trending section is shifted back and forth across the cube. Then the east-west–trending section is shifted. Last of all the horizontal section is raised and lowered through the display cube's extent.

** *Further scales of results also delivered.*

Magnetic 3D structure detection results images

▶ Flat 3D structures — Point set results view

Jaxon_mvi_amp_uniZ_Struct140_Flat_pts

Figure 30: Movie (MP4, 188KB, 10 sec) of a representative image** showing the 140m-scale flat 3D structures detected in the Netalzul Mountain magnetic inversion model. These point set results are shown looking toward the northeast, with a viewing inclination of 11°. This movie's Geoscience Analyst stills are:

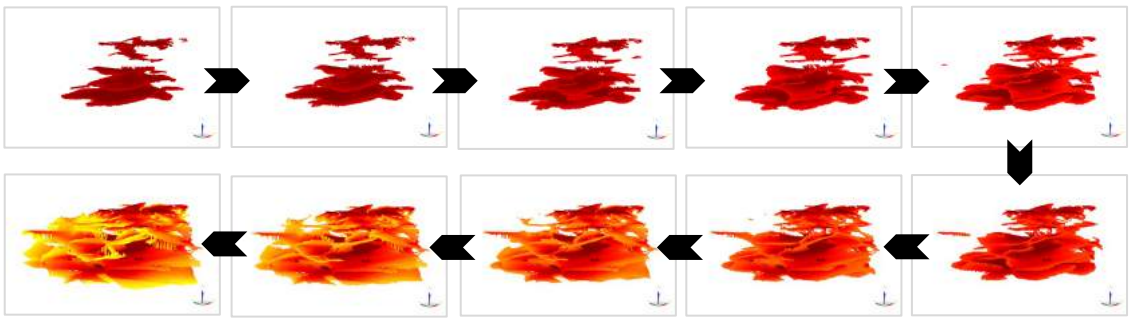

** *Further scales of results also delivered.*

Magnetic 3D structure detection results images

▶ Total 3D structure — Voxel grid in section view

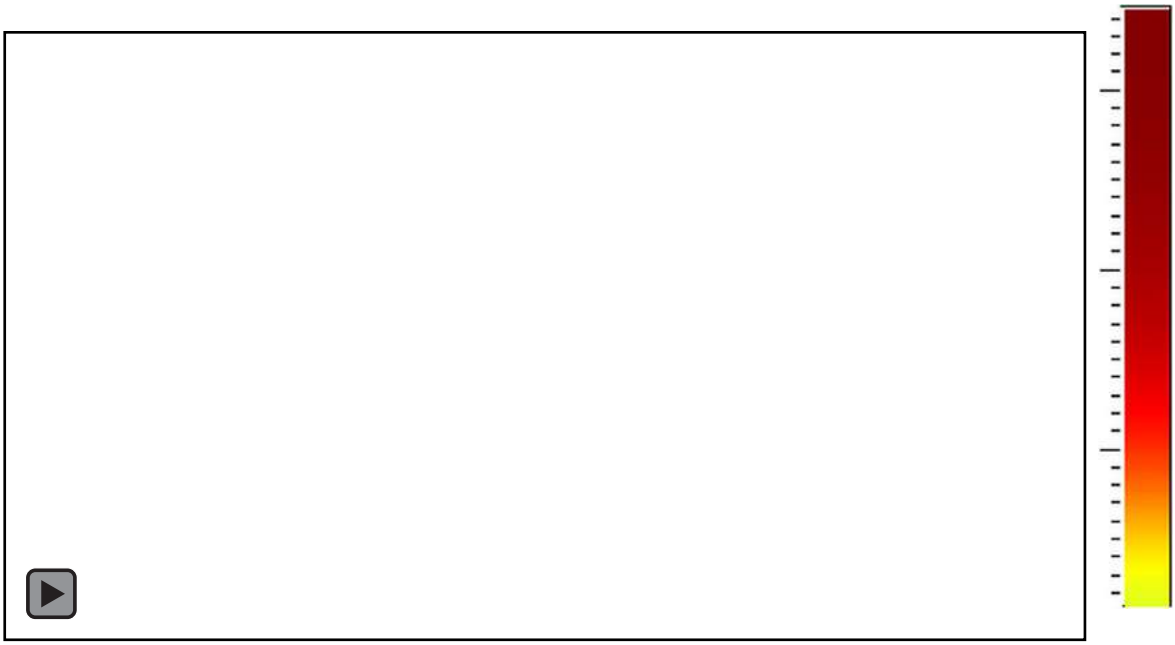

Jaxon_mvi_amp_uniZ_Struct140_Total

Figure 31: Movie (MP4, 2.2MB, 29 sec) of a representative image** showing the 140m-scale total 3D structure network detected in the Netalzul Mountain magnetic inversion model. This voxel grid result is shown looking toward the northeast, with a viewing inclination of 45°. This a movie of the Geoscience Analyst graphic user interface. First, the north-south–trending section is shifted back and forth across the cube. Then the east-west–trending section is shifted. Last of all the horizontal section is raised and lowered through the display cube's extent.

** *Further scales of results also delivered.*

Structural interpretation images

▶ Attributed interpreted stucture — Over analytic signal

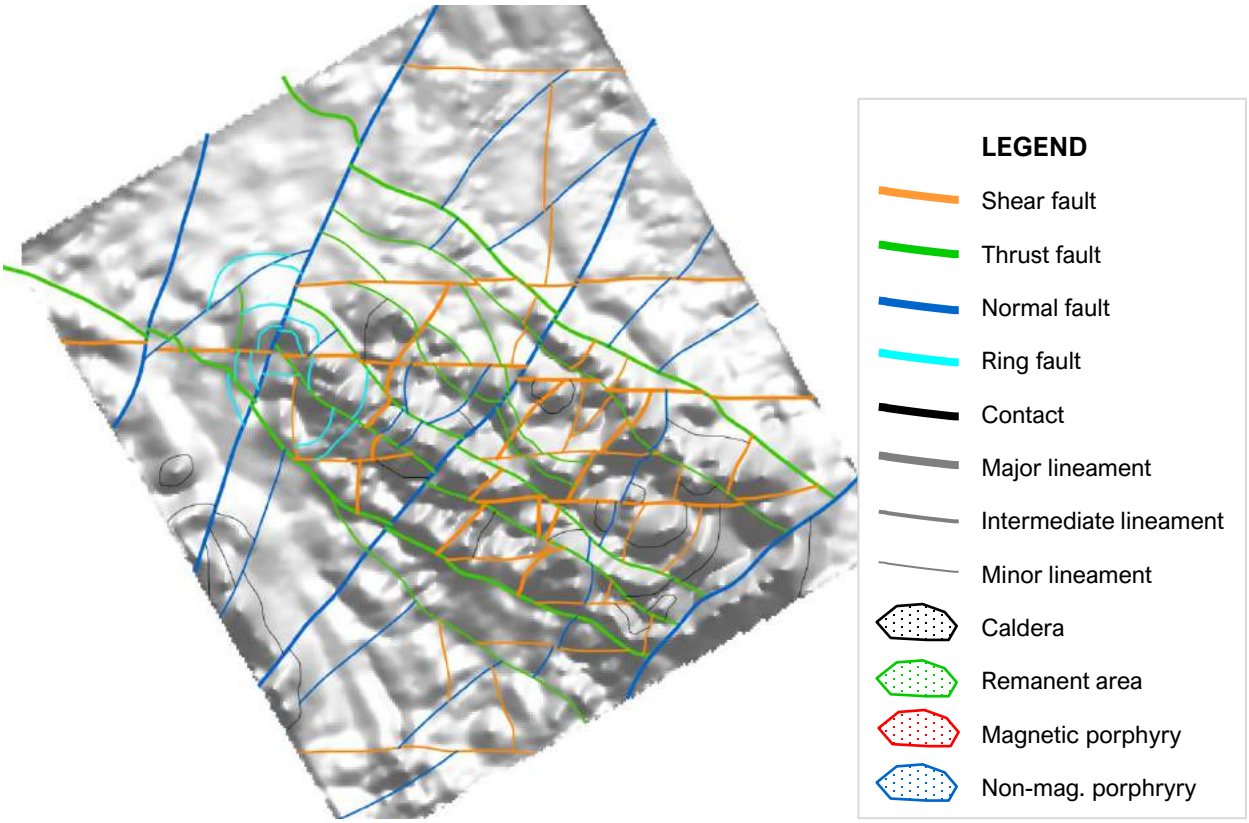

Netalzul_FG_Interp_Structure_Attributed

Figure 32: Structural interpretation of the magnetic data over the Netalzul area colored as indicated in the legend. **Figures 37 to 39** show examples of the different types of structures.

Structural interpretation images
▶ Intepreted remanent areas — Over analytic signal

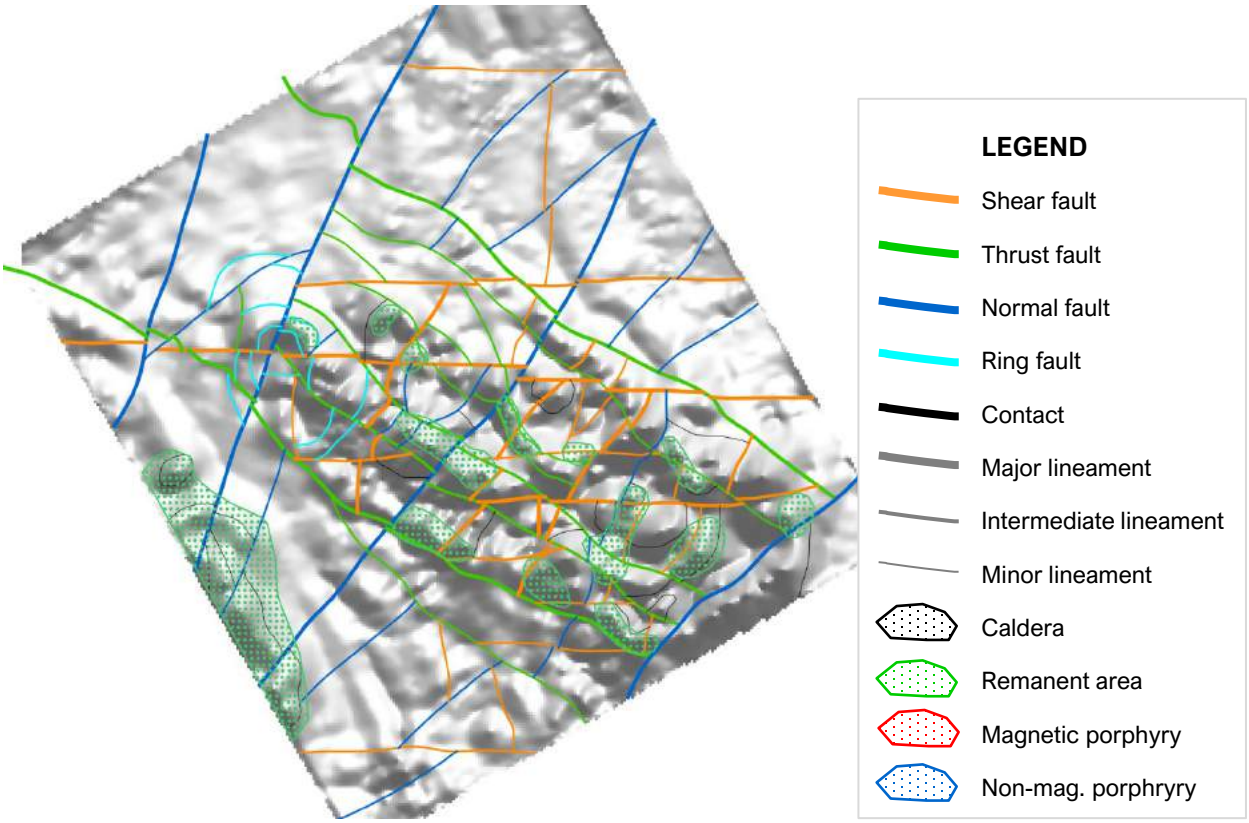

Netalzul_FG_Interp_Remanent_Areas

Figure 33: Remanently magnetized areas are shown as green stippled polygons over the structure interpretation. The remanence is complex and ranges from nearly reversely magnetized to oblique to the present day magnetic field.

Structural interpretation images
▶ Interpreted magnetic porphyry centers — Over analytic signal

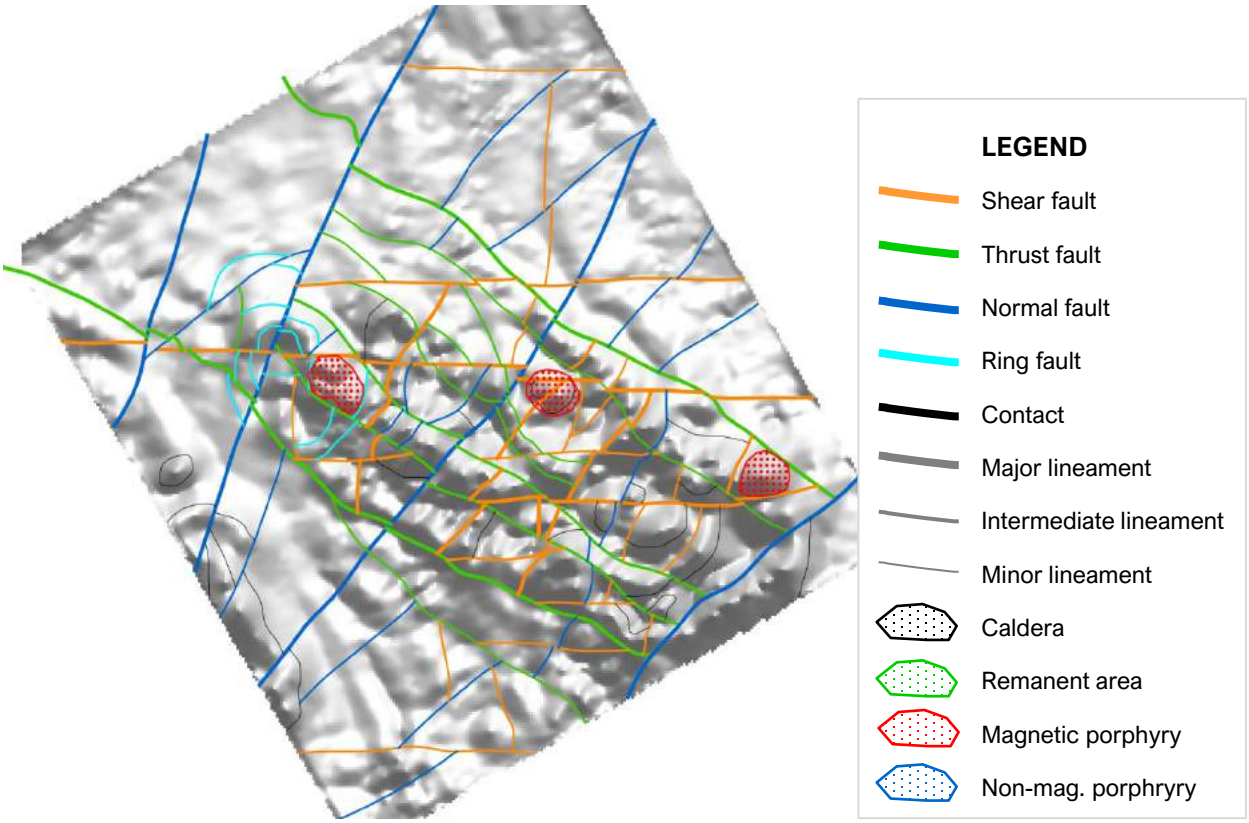

Netalzul_FG_Interp_Porphyry_Centers_Magnetic

Figure 34: Small magnetic anomalies that appear to be caused by high-level intrusions are indicated by red stippled areas over the structural interpretation. These appear to be late intrusive phases but could also be a preserved core of a porphyry system.

Structural interpretation images

▶ Interpreted non-magnetic porphyry centers — Over analytic sig.

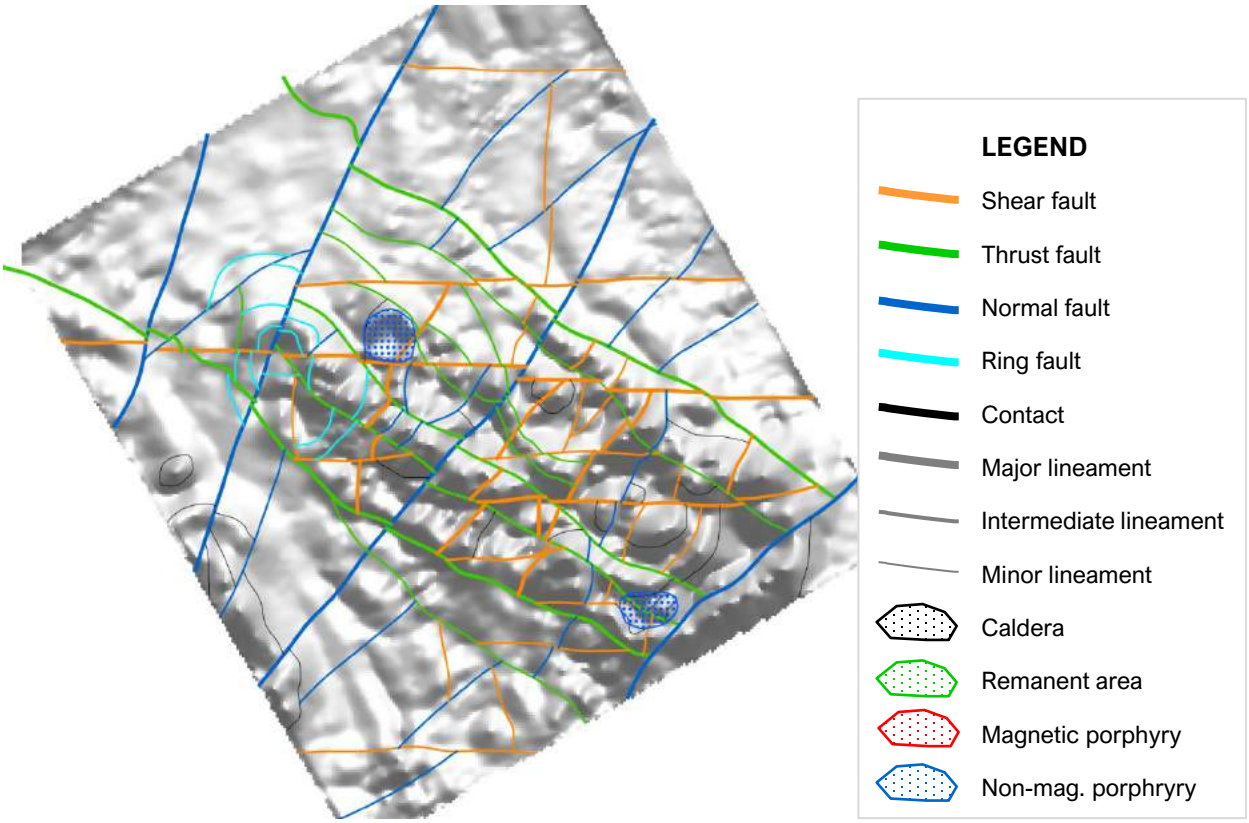

Netalzul_FG_Interp_Porphyry_Centers_Non-Magnetic

Figure 35: Round non-magnetic features are shown as blue stippled areas over the structural interpretation. Discrete non-magnetic zones can be related to magnetite destruction that occurs during phyllic alteration. The highlighted area in the north is coincident with a target generated from the rock geochemical data.

Structural interpretation images
▶ Interpreted caldera — Over analytic signal

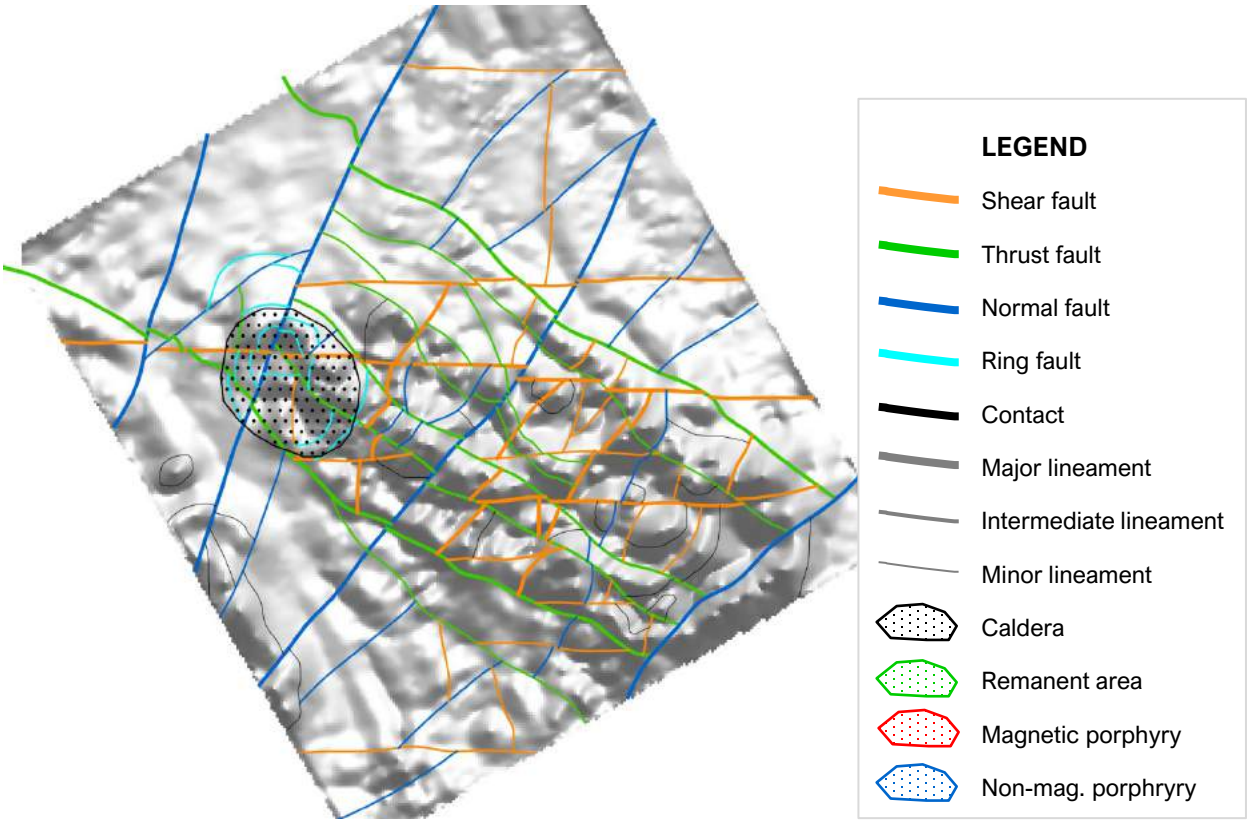

Netalzul_FG_Interp_Caldera

Figure 36: The area in the northeast of the intrusion has apparent ring structures in the analytic signal of the RTP data. This sort of structure can be indicative of collapse after a volcanic eruption. The possible caldera is indicated by black stippling over the structure interpretation.

Structural interpretation images

▶ Strike-slip fault example

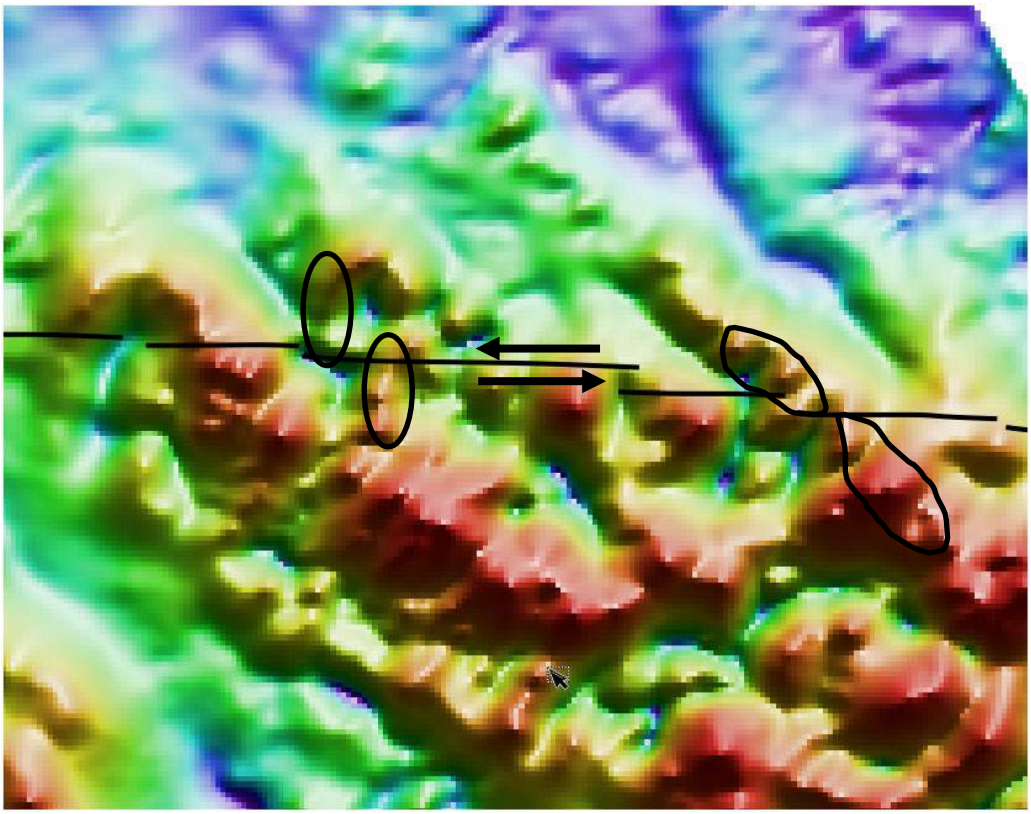

Figure 37: Strike-slip faults are nearly vertical and show lateral offset of units. The fault shown above appears to have around 400-500m of left-lateral displacement. The dip is nearly vertical based on the 3D structure detection, indicating that it is likely a shear zone. The structure appears to play an important role in controlling the distribution of the intrusive rocks in the area. Most of them occur between this fault and the thrust fault shown in **Figure 38**. The structure appears to be relatively early as it is offset by later northwest-trending structures. That is why the fault steps to the north as you go from east to west.

Structural interpretation images
▶ Normal fault example

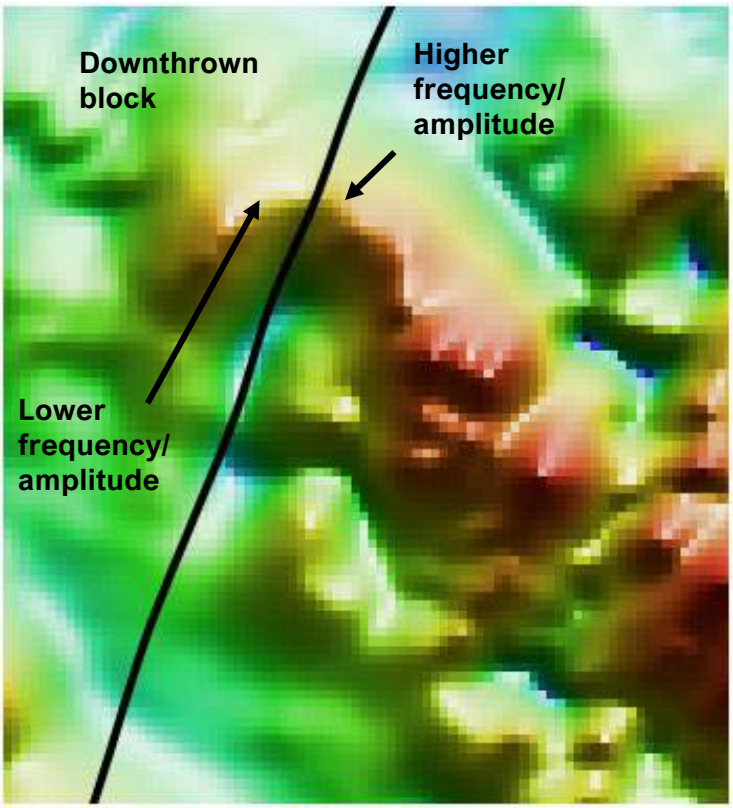

Figure 38: Normal faults with relatively small displacement are relatively steeply dipping faults that have little to know lateral offset across the fault. Instead, the signature is a change in wavelength and/or signal amplitude across a linear feature. In the above example, the features east of the fault are higher amplitude and higher frequency. Across the fault, the main feature is in roughly the same location, but it is lower frequency and lower amplitude suggesting it is down-dropped. This would suggest that the fault dips to the west-northwest. Most of the major normal faults in the area appear to have a similar orientation and offset.

Structural interpretation images
▶ Thrust fault example

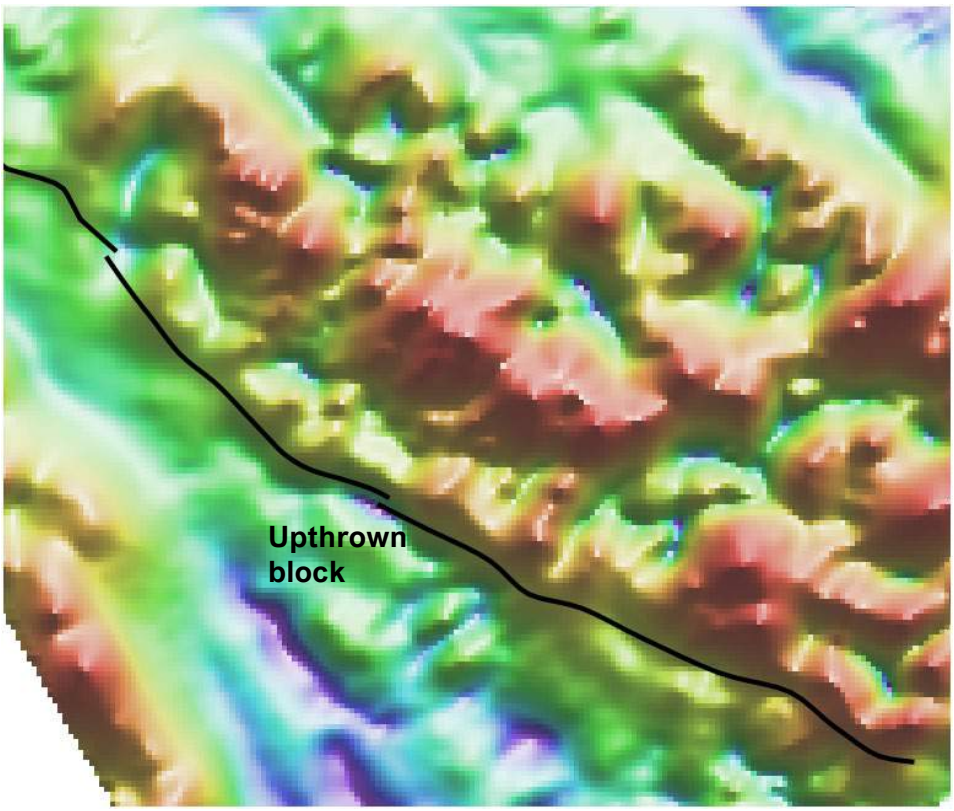

Figure 39: Thrust faults often have a relatively shallow dip and an irregular surface trace. The structure shown here appears to dip to the southwest indicating that the southwest block has been thrust over the northeast block.

Porphyry targeting figures
▶ FG-NZ-Soils-1

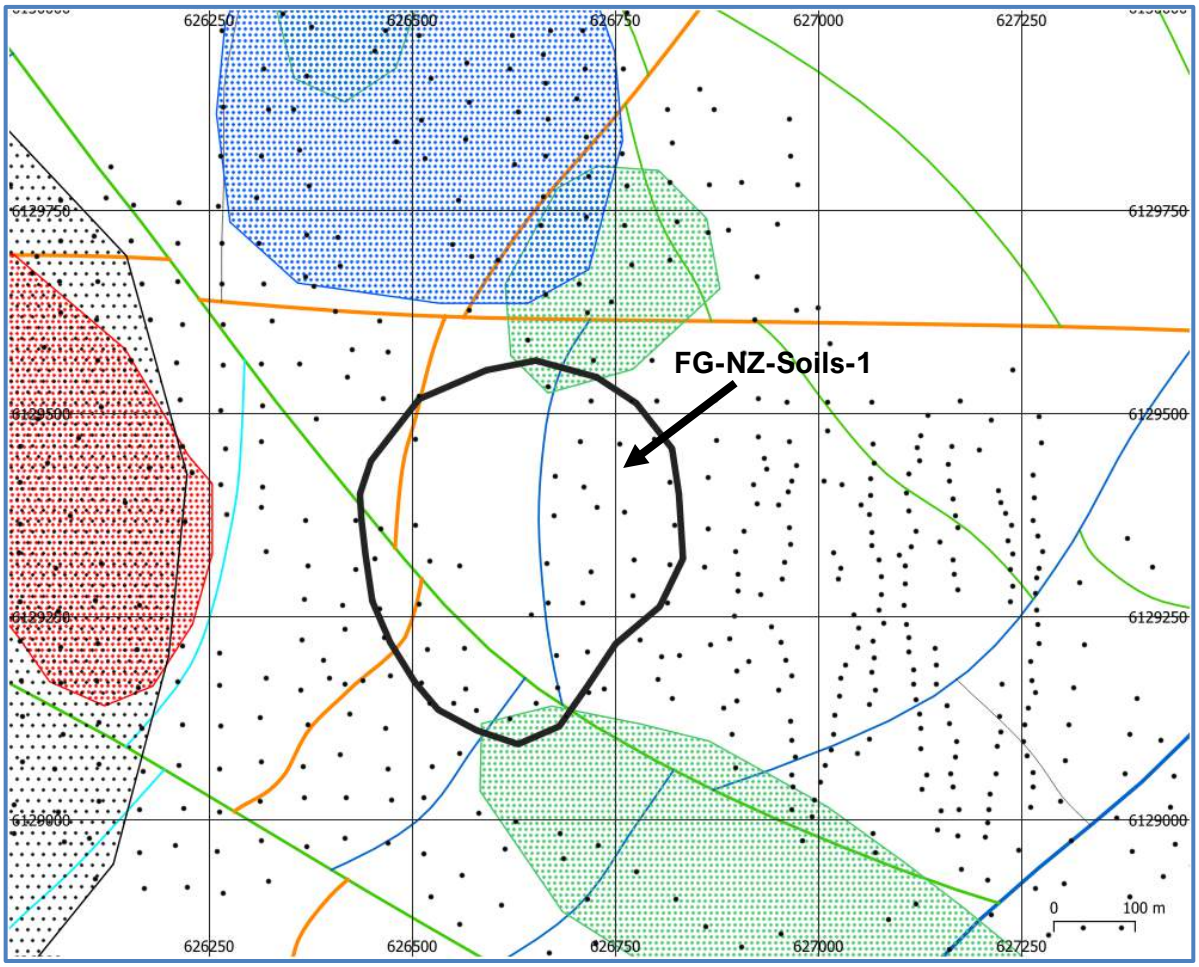

Figure 40: The black line indicates the surface trace of target FG-NZ-Soils-1 from the geochemical footprint modeling. The target is in an area where an apparent thrust fault intersects cross cutting strike-slip and normal faults. The closest anomaly that looks like a discrete intrusion is the remanent anomaly just north of the target. The eastern part of the target is covered with soil samples while the western side has some significant gaps. Filling in the gaps would improve the quality of the depth estimates for the target. Particularly if tin analyses can be included.

Porphyry targeting figures
▶ FG-NZ-Rocks-1

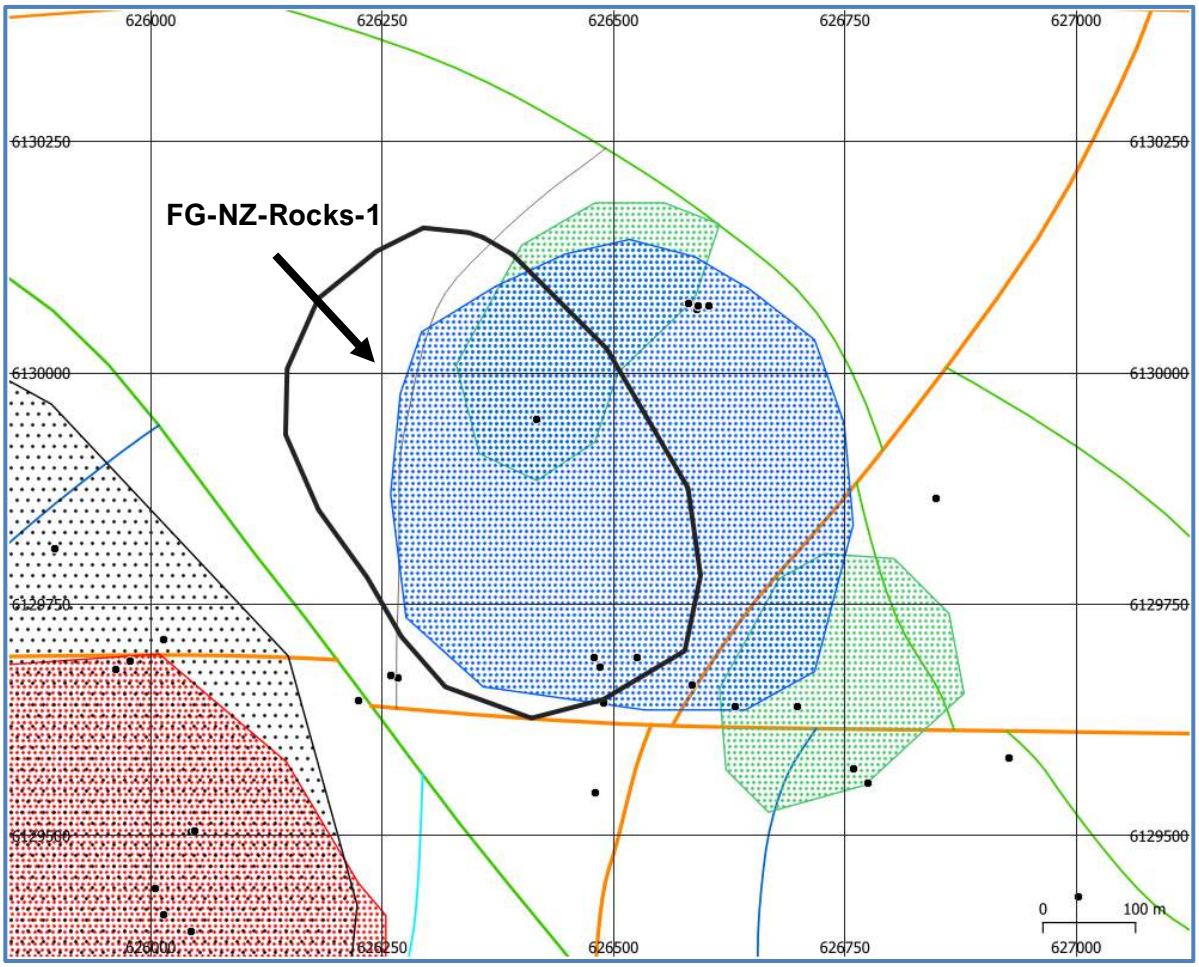

Figure 40: The black line indicates the surface trace of geochemical footprint modeling target FG-NZ-Rocks-1. The target is coincident with a demagnetized zone indicated by the blue stippled area. The target outline is poorly constrained. The black dots indicate the rock sample locations showing that the whole target only has four samples in it and most are at the southern edge. Additional sampling would be useful for determining the merit of the target. The coincidence with a discrete demagnetized zone makes this a high priority target.

Porphyry targeting figures

▶ FG-NZ-Rocks-2, FG-NZ-Rocks-3

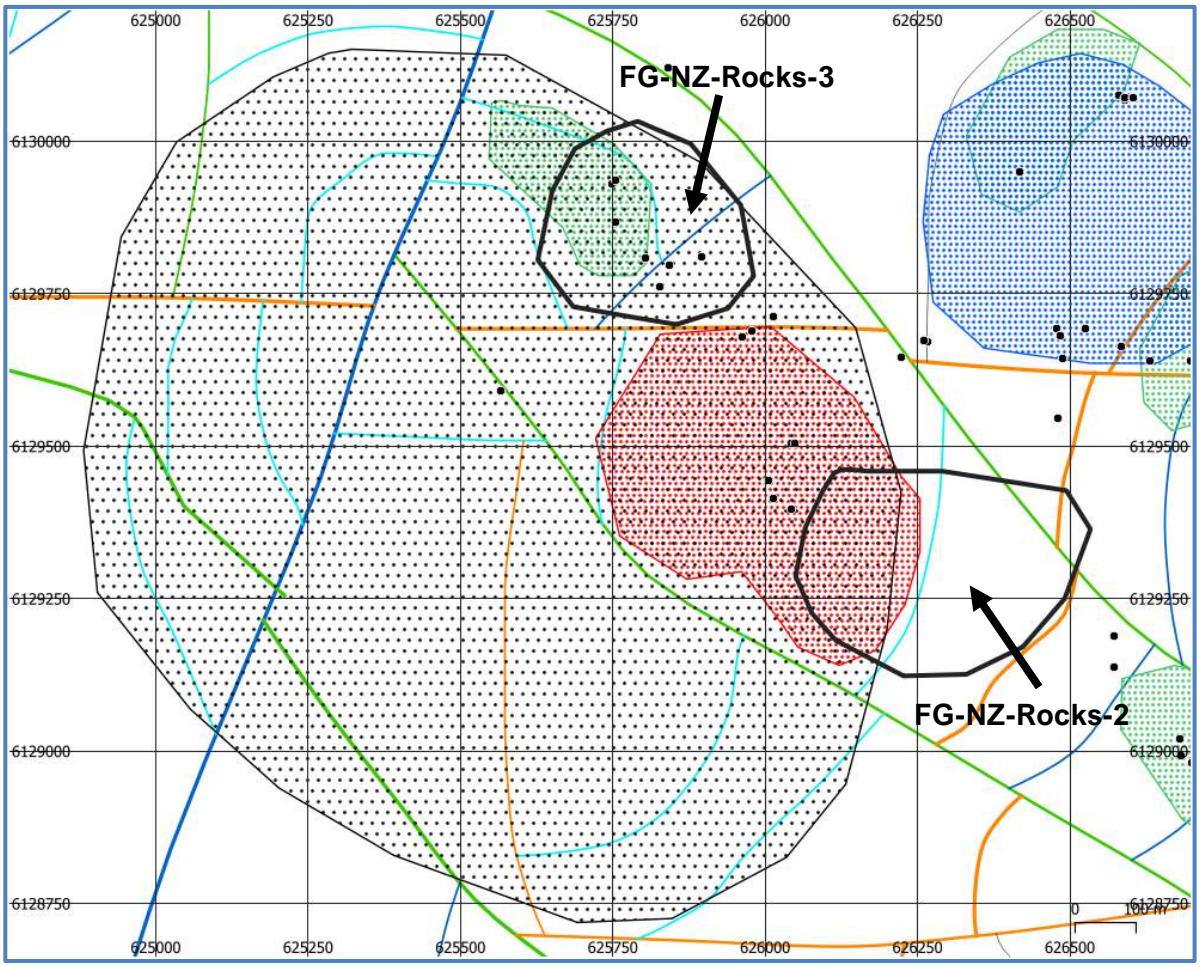

Figure 40: Geochemical footprint modeling targets FG-NZ-Rocks-2 and FG-NZ-Rocks-3 are lower priority targets that are located around the edge of the interpreted caldera shown in black stippling. FG-NZ-Rocks-2 is also partially coincident with a discrete magnetic intrusion shown as a stippled red area. FG-NZ-Rocks-3 has a handful of samples inside the target, but a wider distribution would be required to constrain the bounds and depth of the target better. FG-NZ-Rocks-2 looks interesting geophysically but has no geochemistry samples directly inside the target area.

Appendix 1: Structure detection algorithm

The goal in developing structure detection was to move towards automated interpretation of potential field data that would be most similar to an interpretation by a person. The structure detection is a phase congruency algorithm based on oriented exponential filters (**Kovesi, 1999**).

The structure detection filter is a feature detection algorithm used to highlight ridges, valleys or edges in gridded data. The results are significantly different from other feature detection routines.

Perhaps the biggest difference is that the results are a measure of symmetry or asymmetry, irrespective of amplitude. This is because the analysis is completed using the local phase rather than the signal amplitude.

This means that features in areas of low contrast are highlighted just as well as those in areas of high contrast, as long as the frequencies are present. High values in the structure grid indicate that the structure is close to a step edge. A small step change will have a higher value than a higher amplitude change that is more gradual.

The method is also multi-scale by design. For structures to be highlighted, they must be present at more than one scale. This eliminates more-minor edges that may be present over a narrow frequency range.

The use of exponential filters to determine the scale allows for some inference as to the depth of the structures detected when the filter is applied to potential field data. The wavelength in the filename is the shallowest upward continuation level used and the approximate depth should range between 0.5 and 1 times this wavelength.

This depth estimate is based on **Jacobsen (1987)**. This method is not perfect at separating sources from different depths. It is possible to generate long-wavelength features from shallow sources as evidenced by the fact that there are long wavelength features present in radiometric data, which do not have a significant depth component. However, the method should provide a good first pass estimate of which features extend to depth and which are only surficial. It is possible for deep tapping structures to be missed if there is not a significant property contrast across them.

Appendix 1: Structure detection algorithm (continued)

The structure detection filter produces orientation grids that show the orientation of the strongest edge at a given location. When these orientation grids have been thresholded to remove low amplitude features, it's easier to see the prominent structural orientations.

References

Kovesi, P., 1999, Image Features From Phase Congruency. Videre: A Journal of Computer Vision Research, v. 1, no. 3.

Jacobsen, B.H., 1987, A case for upward continuation as a standard separation filter for potential-field maps. Geophysics, v.52, no. 8, pp. 1138-1148.